

1 **Revisiting *Cryptococcus* extracellular vesicles properties and their use as**
2 **vaccine platforms**

3

4 Juliana RIZZO^{1#}, Sarah Sze Wah WONG², Anastasia D. GAZI³, Frédérique MOYRAND^{1#},
5 Thibault CHAZE⁴, Pierre-Henri COMMERE⁵, Sophie NOVAULT⁵, Mariette MATONDO⁴,
6 Gerard PEHAU-ARNAUDET³, Flavia C. G. REIS^{6,7#}, Matthijn VOS⁸, Lysangela R
7 ALVES^{6#}, Robin C. MAY^{9#}, Leonardo NIMRICHTER^{10#}, Marcio L. RODRIGUES^{6,10#},
8 Vishukumar AIMANIANDA² and Guilhem JANBON^{1##*}

9

10 ¹ Unité Biologie des ARN des Pathogènes Fongiques, Département de Mycologie, Institut Pasteur, F-
11 75015, Paris, France

12 ² Unité Mycologie Moléculaire, CNRS UMR2000, Département de Mycologie, Institut Pasteur, F-
13 75015, Paris, France

14 ³ Ultrastructural Bio-Imaging, UTechS UBI, Département de Biologie cellulaire et infection, UMR
15 3528 CNRS, Institut Pasteur, F-75015, Paris, France

16 ⁴ Plateforme Protéomique, Unité de Spectrométrie de Masse pour la Biologie (MSBio), Centre de
17 Ressources et Recherches Technologiques (C2RT), UMR 2000 CNRS, Institut Pasteur, Paris, France

18 ⁵ Cytometry and Biomarkers, Centre de Ressources et Recherches Technologiques (C2RT), Institut
19 Pasteur, F-75015, Paris, France

20 ⁶ Instituto Carlos Chagas, Fundação Oswaldo Cruz (FIOCRUZ), Curitiba, Brazil

21 ⁷ Centro de Desenvolvimento Tecnológico em Saúde (CDTS-Fiocruz), Brazil

22 ⁸ NanoImaging Core Facility, Centre de Ressources et Recherches Technologiques (C2RT), Institut
23 Pasteur, F-75015, Paris, France

24 ⁹ Institute of Microbiology and Infection and School of Biosciences, University of Birmingham,
25 Birmingham B15 2TT, United Kingdom

26 ¹⁰ Instituto de Microbiologia Paulo de Góes (IMPG), Universidade Federal do Rio de Janeiro, Rio de
27 Janeiro, Brazil

28 [#] Members of the data sharing transparency group on fungal extracellular vesicles

29 * Corresponding author: janbon@pasteur.fr

31

32

33 **Abstract**

34

35 Whereas extracellular vesicle (EV) research has become commonplace in different
36 biomedical fields, this field of research is still in its infancy in mycology. Here we provide a
37 robust set of data regarding the structural and compositional aspects of EVs isolated from the
38 fungal pathogenic species *Cryptococcus neoformans*, *C. deneoformans* and *C. deuterogattii*.
39 Using cutting-edge methodological approaches including cryogenic electron microscopy and
40 cryogenic electron tomography, proteomics, and flow cytometry, we revisited cryptococcal
41 EV features and suggest a new EV structural model, in which the vesicular lipid bilayer is
42 covered by mannoprotein-based fibrillar decoration, bearing the capsule polysaccharide as its
43 outer layer. About 10% of the EV population is devoid of fibrillar decoration, adding another
44 aspect to EV diversity. By analyzing EV protein cargo from the three species, we
45 characterized the typical *Cryptococcus* EV proteome. It contains several membrane-bound
46 protein families, including some Tsh proteins bearing a SUR7/PalI motif. The presence of
47 known protective antigens on the surface of *Cryptococcus* EVs, resembling the morphology
48 of encapsulated virus structures, suggested their potential as a vaccine. Indeed, mice
49 immunized with EVs obtained from an acapsular *C. neoformans* mutant strain rendered a
50 strong antibody response in mice and significantly prolonged their survival upon *C. neoformans*
51 infection.

52

53 **Keywords:** *Cryptococcus*, fungal infections, extracellular vesicles, mannoproteins, vaccine,
54 Cryo-EM

55

56

57

58

59 **1. Introduction**

60 All living organisms release lipid bilayer-delimited particles defined as extracellular
61 vesicles (EVs) (Deatherage and Cookson 2012, Witwer and Théry 2019). EV size ranges from
62 20 nm to close to one micrometer in diameter. In mammalian cells, two major classes of EVs
63 have been defined, microvesicles and exosomes, according to their size and cellular origin
64 (Meldolesi 2018, van Niel et al. 2018). In these organisms, a large body of literature describes
65 how EVs participate in intercellular signaling within and in organism-to-organism
66 communication, including carcinogenesis and host-pathogen interactions (Xu et al. 2018,
67 Shopova et al. 2020). In fungi, the first report of fungal EVs was published in 2007
68 (Rodrigues et al. 2007), and, since then, their existence has been reported in many species of
69 pathogenic and nonpathogenic fungi (Rizzo et al. 2020).

70 By analogy with mammalian EVs, it has been hypothesized that fungal EVs could also
71 participate in many biological processes (Rodrigues and Casadevall 2018). Indeed, some
72 reports indicate their relevance in diverse mechanisms related to fungal pathophysiology, such
73 as antifungal resistance and biofilm formation (Leone et al. 2018, Zarnowski et al. 2018),
74 transfer of virulence-associated molecules and modulation of host cells (Oliveira et al. 2010,
75 Vargas et al. 2015, Rizzo et al. 2017, Bielska et al. 2018, Souza et al. 2019, Hai et al. 2020),
76 cell wall remodeling and biogenesis (Zhao et al. 2019, Rizzo et al. 2020), among others
77 (Bielska and May 2019, Rizzo et al. 2020). Nevertheless, the molecular mechanisms
78 implicated in these exchanges of information, as well as the genetics regulating fungal EV
79 biogenesis and release, remain elusive.

80 As with their mammalian, bacterial and plant counterparts, fungal EVs have been
81 shown to contain proteins, pigments, nucleic acids, polysaccharides, lipids, among other
82 molecules (Eisenman et al. 2009, Vallejo et al. 2012, da Silva et al. 2015, Rodrigues et al.
83 2015, Joffe et al. 2016, Rayner et al. 2017, Reis et al. 2021). Besides the claudin-like Sur7
84 family proteins, recently suggested as EV protein markers in *Candida albicans* (Dawson et al.
85 2020), no other fungal EV specific molecular marker has been reported. Indeed, the laborious
86 and inefficient EV isolation protocols that have been used until recently have strongly limited
87 the knowledge on their composition. Additional hurdles regarding purification methods
88 potentially affect an accurate vesicular compositional characterization (Théry et al. 2018),
89 including potential carryover contaminants such as protein aggregates (Chiou et al. 2018).
90 Regarding EV morphological diversity, previous studies have reported the heterogeneity of
91 fungal EV size, as recently reviewed (Bielska and May 2019). However, single particle
92 analyzers such as the widely used Nanoparticle Tracking Analysis (NTA) and most common

93 flow cytometers cannot reliably evaluate particles smaller than 100 nm in diameter (Maas et
94 al. 2015, Théry et al. 2018, Chiang and Chen 2019, Noble et al. 2020). Overall, although a
95 considerable number of fungal EV-related studies have been published in recent years, our
96 knowledge of fungal EV structure and composition remains limited, which prevents further
97 robust analysis of their functions.

98 Seven species of pathogenic *Cryptococcus* have been described (Hagen et al. 2015).
99 Whereas species belonging to the *neoformans* clade (*C. neoformans* and *C. deneoformans*)
100 typically affect immunocompromised patients, species belonging to the *gattii* clade (*C. gattii*,
101 *C. deuterogattii*, *C. tetragattii*, *C. decagattii*, and *C. bacillisporus*) are often primary
102 pathogens and can cause aggressive pulmonary infections as well as meningoencephalitis
103 (Kwon-Chung et al. 2014, Rajasingham et al. 2017, Janbon et al. 2019). *C. neoformans* has
104 historically been one of the most studied fungi regarding EV biology (Rodrigues et al. 2007,
105 Bielska and May 2019, Rizzo et al. 2020). However, the only structural analyses of EVs from
106 this organism are now very outdated and technologies used have shown tremendous
107 improvements since then (Emelyanov et al. 2020, Noble et al. 2020).

108 To date, *Cryptococcus* EV proteomic approaches have identified 92 and 202 proteins,
109 with very poor overlap and no evaluation of their abundance or enrichment (Rodrigues et al.
110 2008, Wolf et al. 2014). Finally, although the current model of fungal EV structure contains
111 proteins located on the vesicular surface (by analogy with the mammalian EV structures
112 (Emelyanov et al. 2020, Noble et al. 2020)), more experimental evidence is necessary to
113 identify these putative membrane-associated molecules. Since many immunogenic proteins
114 are often found to be associated with EVs, their vaccine potential has been explored mostly
115 for bacterial and parasitic infections (Coakley et al. 2017, Wang et al. 2018), and more
116 recently also for fungal infections (Colombo et al. 2019, Vargas et al. 2020).

117 In the present study, we used the recently described protocol (Reis et al. 2019) to
118 obtain EV-enriched samples from *Cryptococcus*, together with cutting edge methodological
119 approaches to revisit *Cryptococcus* EV structure, cargo, and their biological functions. Here
120 we report a detailed analysis of three species (*C. neoformans*, *C. neoformans* and *C.
121 deuterogattii*) for which both a good genome annotation and RNA-Seq data were available
122 (Janbon et al. 2014, Gonzalez-Hilarion et al. 2016, Gröhs Ferrareze et al. 2021). We produced
123 a robust set of data containing cryo-electron microscopy (cryo-EM) and cryo-electron
124 tomography (cryo-ET) proteomics, and nanoscale flow cytometry analysis, suggesting a new
125 EV structural model, in addition to a list of cryptococcal EV protein markers. Our results led

126 us to further evaluate the EV biological roles in murine models, emphasizing their potential
127 use as an anti-cryptococcosis vaccine.

128

129 **2. Material and Methods**

130

131 **Strains and media**

132 The wild type strains used in the study were *C. neoformans* strain KN99α, *C. deneoformans*
133 strain JEC21, *C. deuterogattii* strain R265, *C. albicans* strain SC5314, and *S. cerevisiae* strain
134 S288C. The *C. neoformans* strain NE367 (*MATα cap59Δ::NAT*) has been previously
135 described (Moyrand et al. 2007). The strains *MATα vep1Δ::NAT* (CNAG_03223), *MATα*
136 *hoc3Δ::NAT* (CNAG_00158), *MATα alg3Δ::NAT* (CNAG_05142), *MATα ktr3Δ::NAT*
137 (CNAG_03832) have been constructed in the Hiten Madhani lab (UCSF, USA) and obtained
138 from the Fungal Genetic Stock Center. To construct the strains NE1281 (*MATα*
139 *mp88Δ::NEO*) and NE1469 (*MATα vep1Δ::NAT mp88Δ::NEO*), we replaced the entire
140 CNAG_00776 (*MP88*) CDS by the *NEO* marker in the strains KN99α and *MATα*
141 *vep1Δ::NAT*, respectively. We here followed the previously described CRISPR CAS9 method
142 (Fan and Lin 2018). The plasmid pPZP-NEO1 used to amplify the *NEO* selective marker was
143 kindly provided by Dr. Joseph Heitman (Duke University). The deletion cassettes was
144 constructed using a strategy previously applied to *Neurospora crassa* (Collopy et al. 2010).
145 The transformants were then screened for homologous integration, as previously described
146 (Moyrand et al. 2007). Two representatives independently obtained mutant strains were
147 stocked at -80°C. All primer sequences used are provided in Table S1. All strains were taken
148 from the G. Janbon laboratory collection at -80°C, plated on yeast extract-peptone-dextrose
149 (YPD) and incubated at 30°C for 48h before each experiment.

150

151 **EV isolation, labelling and proteinase K treatment**

152 EV purification was based on the recently published protocol (Reis et al. 2019) with
153 some modifications. One loop of cells was inoculated into 10 mL of liquid YPD and
154 incubated at 30°C for 24h with shaking (150 rpm). Cells were washed twice with 10 ml of
155 sterile water, counted and diluted to a density of 3.5×10^7 cells/mL in water. Aliquots of 300
156 μ L of the cellular suspension were spread onto synthetic dextrose (SD) solid medium plates
157 and incubated for 24 h at 30°C to reach cell confluence. The cells were recovered from each
158 plate with a 10 μ L inoculation loop and transferred to an ultracentrifugation tube containing

159 10 mL 0.22 μ m-filter sterile of 0.01 M PBS. Cells were homogenized and collected by
160 centrifugation at 5,000 x g for 15 min at 4°C. Supernatants were collected and centrifuged
161 again at 15,000 x g for 15 min at 4°C to eliminate cellular debris. The resting supernatants
162 were filtered through 0.45 μ m syringe filters and ultracentrifuged at 100,000 x g for 1h at 4°C
163 (SW41 Ti swinging-bucket rotor, Beckman Coulter). The supernatant was discarded and the
164 pellet suspended in 0.22 μ m-pore filtered or 0.02 μ m-pore filtered (for Flow Cytometry
165 analysis) PBS for immediately use or stored at -80°C for further experiments. The amount of
166 total sterol in the EV samples was measured by the Amplex™ Red Cholesterol Assay Kit
167 (ThermoFisher, A12216) and adjusted for the subsequent experiments.

168 EVs were labelled either with the Concanavalin A (ConA) - Alexa Fluor™ 488
169 conjugated, or with the Alexa 488 labelled anti-GXM monoclonal antibody 18B7 (Casadevall
170 et al. 1992), a kind gift of Oscar Zaragoza. The ConA stock solution (5mg/mL) was
171 previously centrifuged at 13.000 x rpm for 2 min, in order to eliminate possible aggregates,
172 and diluted to 500 μ g/mL in filtered PBS. In 1.5 mL Eppendorf tubes, 5 μ L of ConA (500
173 μ g/mL), together with 5 μ L EV suspension were add to a final volume of 100 μ L filtered
174 PBS. The tubes were incubated for 1 h at 30°C, under agitation and protected from light.
175 After incubation, 10 mL of 0.02 μ m-pore filtered PBS were added to the EV suspension and
176 then submitted to ultracentrifugation for 1 h at 100 000 x g at 4°C. The supernatant was again
177 discarded and pellets suspended in 300 μ L of 0.02 μ m-pore filtered before being transferred
178 to BD Trucount™ Tubes (BD Biosciences) and proceeded to Flow Cytometry analysis. A
179 similar protocol was applied for the EV labelling with the Alexa 488 labelled anti-GXM
180 monoclonal antibody 18B7, which was diluted 20 times before adding to EV suspension.

181 EV proteinase K treatment was performed following the previously described
182 protocol (Yang et al. 2021) with some modifications. Briefly, proteinase K was added to the
183 EV suspension (0.17 μ g of sterol) to a final concentration of 2 mg/mL in 0.02 μ m-pore
184 filtered PBS. After proteolysis for 1h at 55°C under agitation (300 rpm), the enzymatic
185 reaction was stopped by the proteinase inhibitor PMSF (1 mM) for 20 min at RT. Proteinase
186 K treated EVs were finally submitted to ConA labelling, ultracentrifuge washed as described
187 before and analyzed by flow cytometry. Control conditions included untreated EVs and EVs
188 incubated only with PMSF.

189

190 **Flow cytometry**

191 EVs were analyzed and sorted on a cell sorter MoFlo Astrios (Beckman Coulter)
192 equipped with an EQ module specifically developed to detect nanoparticles and with 488 nm

193 and 561 nm lasers at 200 mW. The sorting was carried out with a 70 μ m nozzle at a pressure
194 of 60 PSI and a differential pressure with the sample of 0.3-0.4 PSI. The sheath liquid NaCl
195 0.9% (REVOL, France) was filtered on a 0.04 μ m filter. The analyses were on the SSC
196 parameter of laser 561, with threshold set to 0.012% in order to have maximum 300 eps. An
197 M2 mask was added in front of the FSC. All SSC and FSC parameters are viewed in
198 logarithmic mode. The calibration of the machine was carried out using Megamix-Plus SSC
199 beads from BioCytex. We used the TrucountTM Tubes to normalize the EV counting for ConA
200 labelling, and the fluorescence of the Mab18B7 and alexa 488 conjugated, and beads
201 TrucountTM was measured on parameter 488-513/26. Control conditions including
202 ultracentrifuge washed PBS, previously incubated with ConA were used to evaluate the PBS
203 associated noise and to normalize labelling percentages. Flow Cytometry data were analyzed
204 by FlowJo V10 Software.

205

206 **Nanoparticle tracking analysis (NTA)**

207 Quantitative determination of EV size distribution was performed by NTA, in addition
208 to microscopic methods. Protocols that were recently established for the analysis of
209 cryptococcal EVs were used (Reis et al. 2019). Briefly, ultracentrifugated pellets were 20- to
210 50-fold diluted in filtered PBS and measured within the optimal dilution range of 9×10^7 to
211 2.9×10^9 particles/mL on an LM10 nanoparticle analysis system, coupled with a 488-nm laser
212 and equipped with an SCMS camera and a syringe pump (Malvern Panalytical, Malvern,
213 United Kingdom). The data were acquired and analyzed using the NTA 3.0 software (Malvern
214 Panalytical).

215

216 **Cryo-EM and cryo-ET**

217 EVs (4 μ L) were spotted on glow-discharged lacey grids (S166-3, EMS) and cryo-
218 fixed by plunge freezing at -180°C in liquid ethane using a Leica EMGP (Leica, Austria).
219 Grids were observed either with Tecnai F20, or Titan Krios (Thermo Fisher Scientific). The
220 Tecnai F20 (Thermo Fisher Scientific) was operating at 200kV and images were acquired
221 under low-dose conditions using the software EPU (Thermo Fisher Scientific) and a direct
222 detector Falcon II (Thermo Fisher Scientific).

223 Cryo-electron tomography was performed using 5 nm protein-A gold particles (UMC,
224 Utrecht). These were mixed with the sample to serve as fiducial markers for subsequent image
225 alignment. EV sample (4 μ L) was applied to glow discharged Lacey grids (S166-3, EMS)
226 prior plunge-freezing (EMGP, Leica). Initial bi-directional tilt series acquired using a

227 TECNAI F20 transmission electron microscope (FEI) operated at 200kV under parallel beam
228 conditions using a Gatan 626 side entry cryoholder. The SerialEM software (Mastronarde
229 2005, Schorb et al. 2019) was used to automatically acquire images every 2° over a ±45°
230 range using a Falcon II direct detector with a pixel size of 2 Å, using a total dose of 180
231 electrons per Å². At least 100 EV cryo-EM images obtained from TECNAI F20 were used for
232 measuring EV diameter and decoration thickness in wild type (WT) and mutant strains. For
233 each EV, an average of three different measurements were used to calculate the diameter
234 (delimited by the lipid bilayer) and the decoration thickness.

235 Dose-symmetric tilt series were collected on a 300kV Titan Krios (Thermo Scientific)
236 transmission electron microscope equipped with a Quantum LS imaging filter (Gatan, slit
237 with 20 eV), single-tilt axis holder and K3 direct electron detector (Gatan). Tilt series with
238 an angular increment of 2° and an angular range of ±60° were acquired with the Tomography
239 software (Thermo Scientific). The total electron dose was between 120 and 150 electrons per
240 Å² and the pixel size at 3.38 Å. Dose symmetric tilt series were saved as separate stacks of
241 frames and subsequently motion-corrected and re-stacked from -60° to +60° using IMOD's
242 function align frames (Mastronarde and Held 2017) with the help of a homemade bash script.

243 Initial image shifts were estimated using IMOD's function tiltcorr. Alignments were
244 further optimized in IMOD using the tracing of 30-40 gold fiducials across the tilt series. The
245 fiducial models gave an overall of a fiducial error around 6 ± 2.7 Å. In cases of a higher error,
246 local alignments were taken into consideration, to further correct the sample's beam induced
247 motion observed. Three-dimensional reconstructions were calculated in IMOD by weighted
248 back projection using the SIRT-like radial filter to enhance contrast and facilitate subsequent
249 segmentation analysis.

250

251 **EV-modeling and analysis of tomographic data**

252 Tomograms were displayed and analyzed using the 3dmod interface of IMOD
253 (Kremer et al. 1996). EVs were modeled with manual tracing of their great circle prior the use
254 of the spherical interpolator of IMOD. If the elliptical contours calculated could not follow the
255 vesicular membrane adequately, further manual tracing was used before re-applying the
256 interpolator. This involved tracing of membranes near the poles of the vesicles where the
257 membrane information could still be followed. To evaluate and assign diameters to a total of
258 434 *C. neoformans* regular vesicles, located in 39 tomograms, the value of the perimeter of
259 the spheroid's great circle was extracted using the imodinfo function of IMOD, from the same
260 initial manually traced contours used for modelling. To display in 3D the vesicle contour data

261 were meshed using the imodmesh function of IMOD. The projections of the 3D spheroidal
262 models were displayed and rotated to study their 3D geometry.

263 For the evaluation of the decoration thickness, regular vesicles were analyzed by
264 manually measuring the outer EV diameter (delimited by the fibrillar decoration) and the
265 inner diameter (delimited by the lipid bilayer), across the longest axis of the vesicle. The final
266 calculation of the decoration thickness was the subtraction of the inner diameter from the
267 outer diameter, divided by two. For the modeling of the fibrillar decoration, the IMOD surface
268 models were imported to UCSF Chimera (Pettersen et al. 2004). The models were used as
269 masks to extract a slab of data around their outer surface, corresponding to the decoration.
270 The thickness of the slab used refers to the mean value provided by the aforementioned
271 manual analysis. Iso-surface representation of the decoration and final 3D data visualization
272 of the models performed with UCSF Chimera (Pettersen et al. 2004).

273

274 **Immunization assays**

275 The animal experiments were approved by the ethical committee for animal experimentation
276 Comité d'Éthique en Experimentation Animale (CETEA Project license number 2013-0055).
277 Six-week old female BALB/c mice (Janvier Labs) were used for immunization study. The
278 amount of EVs, in protein concentration, was determined by BCA method prior to
279 immunization. Following, three intraperitoneal injections (fixing protein concentration in the
280 EVs to either 1 or 10 µg and suspending in 100 µL PBS) at 15-day intervals were given to the
281 mice. The control group of mice was injected only with PBS. Blood was collected from the
282 submandibular veins of the mice three days after the last immunization and just before the
283 fungal infection and tested for antibody response by Western blot. Briefly, the EVs-associated
284 proteins were separated on 12% SDS-PAGE, and electroblotted to nitrocellulose membrane.
285 By Western blotting, using the mouse sera at dilution 1:1000 and anti-mouse IgG antibody
286 conjugated to peroxidase (Sigma Aldrich), the antibody response specific to the EV-
287 associated proteins was examined. Once the antibody response was confirmed, all the
288 immunized and control mice were challenged intranasally, around one month from the last
289 immunization, with 1×10^4 cells of *C. neoformans* wild-type strain, and their body weights
290 and survival were monitored until all mice succumbed to the infection. The immunization
291 assay was performed in two biological replicates.

292

293 **Vesicle denaturation and protein digestion**

294 EVs proteins were solubilized in urea 8 M, Tris 100 mM pH 7.5, 5 mM tris (2-
295 carboxyethyl) phosphine (TCEP) for 20 min at 23°C. Samples were sonicated using a
296 Vibracell 75186 and a miniprobe 2 mm (Amp 80% // Pulse 10 off 0.8, 3 cycles). Proteins
297 were then alkylated with 20 mM iodoacetamide for 30 min at room temperature in the dark.
298 Subsequently, LysC (Promega) was added for the first digestion step (protein to Lys-C ratio =
299 80:1) for 3h at 30°C. Then samples were diluted down to 1 M urea with 100 mM Tris pH 7.5,
300 and trypsin (Promega) was added to the sample at a ratio of 50:1 for 16h at 37°C. Proteolysis
301 was stopped by adding Formic acid (FA) to a final concentration of 1 % (vol/vol). Resulting
302 peptides were desalted using Sep-Pak SPE cartridge (Waters) according to manufactures
303 instructions.

304

305 **LC-MS/MS of tryptic digest**

306 LC-MS/SM analysis of trypsin-digested proteins (peptides) was performed on an
307 Orbitrap Q Exactive Plus mass spectrometer (Thermo Fisher Scientific, Bremen) coupled to
308 an EASY-nLC 1200 (Thermo Fisher Scientific). A home-made column was used for peptide
309 separation [C₁₈ 40 cm capillary column picotip silica emitter tip (75 µm diameter filled with
310 1.9 µm ReproSil-Pur Basic C₁₈-HD resin, (Dr. Maisch GmbH, Ammerbuch-Entringen,
311 Germany)]. It was equilibrated and peptide was loaded in solvent A (0.1 % FA) at 900 bars.
312 Peptides were separated at 250 nL·min⁻¹. Peptides were eluted using a gradient of solvent B
313 (ACN, 0.1% FA) from 3% to 22 % in 160 min, 22% to 50% in 70 min, 50% to 90% in 5 min
314 (total length of the chromatographic run was 250 min including high ACN level step and
315 column regeneration). Mass spectra were acquired in data-dependent acquisition mode with
316 the XCalibur 2.2 software (Thermo Fisher Scientific, Bremen) with automatic switching
317 between MS and MS/MS scans using a top-10 method. MS spectra were acquired at a
318 resolution of 70000 (at *m/z* 400) with a target value of 3×10^6 ions. The scan range was
319 limited from 300 to 1700 *m/z*. Peptide fragmentation was performed using higher-energy
320 collision dissociation (HCD) with the energy set at 27 NCE. Intensity threshold for ions
321 selection was set at 1×10^6 ions with charge exclusion of z = 1 and z > 7. The MS/MS spectra
322 were acquired at a resolution of 17500 (at *m/z* 400). Isolation window was set at 1.6 Th.
323 Dynamic exclusion was employed within 45 s.

324

325 **Data processing**

326 Data were searched using MaxQuant (version 1.5.3.8 and 1.6.6.0) (Cox and Mann
327 2008, Tyanova et al. 2016) using the Andromeda search engine (Cox et al. 2011) against

328 home-made databases. The following databases were used. For *C. neoformans* KN99a, *C.*
329 *deneoformans* JEC21 and *C. deuterogattii* R265 we used the recently updated proteomes
330 (Wallace et al. 2020, Gröhs Ferrareze et al. 2021). The following search parameters were
331 applied: carbamidomethylation of cysteines was set as a fixed modification, oxidation of
332 methionine and protein N-terminal acetylation were set as variable modifications. The mass
333 tolerances in MS and MS/MS were set to 5 ppm and 20 ppm respectively. Maximum peptide
334 charge was set to 7 and 7 amino acids were required as minimum peptide length. A false
335 discovery rate of 1% was set up for both protein and peptide levels. The iBAQ intensity was
336 used to estimate the protein abundance within a sample (Schwanhäusser et al. 2011).

337

338 **Statistical analysis**

339 All statistical analyses were performed using GraphPad Prism 8 software (GraphPad
340 Software Inc.). Data sets were tested for normal distribution using Shapiro-Wilk or
341 Kolmogorov-Smirnov normality tests. In the cases in which the data passed the normality test,
342 they were further analyzed using the unpaired Student's t test or ordinary one-way ANOVA.
343 When at least one data set was nonnormally distributed, we used the nonparametric
344 Kolmogorov-Smirnov or Kruskal-Wallis test. For the comparison of the survival curves, we
345 used the Logrank (Mantel-Cox) test.

346

347

348 **3. Results**

349

350 **- Diversity of cryptococcal EVs**

351 Several groups have performed morphological studies of fungal EVs by electron
352 microscopy (Rodrigues et al. 2007, Oliveira et al. 2009, Rayner et al. 2017, Bleackley et al.
353 2020). However, most of these studies used sample fixation-dehydration procedures for
354 transmission electron microscopy (TEM), which can often affect the size and morphology of
355 EVs (Van Der Pol et al. 2010, Chiang and Chen 2019). Cryo-EM imaging on rapidly-frozen
356 samples at low temperature could potentially reduce sample damaging and artifacts caused by
357 the addition of heavy metals, dehydration, or fixation steps (Orlov et al. 2017, Chiang and
358 Chen 2019). Indeed, diverse morphologies of EVs derived from even a single mammalian cell
359 type have been clearly revealed under cryo-EM (Zabeo et al. 2017). We therefore used cryo-
360 EM and cryo-ET to analyze EVs purified from *C. neoformans*, in their near-native state.

361 Based on the optimized version of the EV purification protocol recently described by
362 Reis and collaborators (Reis et al. 2019), we isolated EVs from *C. neoformans* reference
363 strain KN99α, cultured on synthetic dextrose solid medium for 24h, in order to limit the
364 carryover of potential contaminants. Cryo-ET tomograms allowed us to analyze 533 single
365 vesicles, which were characterized according to their morphological aspects in regular (round-
366 bilayered vesicles) and irregular (not rounded, bi- or multilayered vesicles) categories.
367 Although a large proportion (81.4%) of the observed EVs had the typical round shape, 18.6%
368 corresponded to irregular morphologies. Among them, we observed examples of multilayered
369 vesicles, long tubular, flat, short tubular and miscellaneous morphologies (**Fig. S1; Table S2**).
370 However, it remains to be determined whether EVs with irregular morphologies are produced
371 biologically or they appear as a consequence of the purification method.

372 Cryo-EM analysis showed a considerable polymorphism of EVs, with the two leaflets
373 of the typical vesicular membrane readily visible for all EVs observed, and a few unstructured
374 aggregates, thus confirming the quality of our preparation (**Fig. 1A**). In *C. neoformans*,
375 among the regular vesicles, only 10.8% appeared to have a smooth surface (**Fig. 1B and 1C**);
376 the majority of regular EVs (89.2%) were decorated with a fibrillar structure anchored to the
377 lipid bilayer (**Fig. 1D and 1E**). Strikingly, regardless of the morphology, the majority of EVs
378 analyzed (88.6%) appeared to be coated with this fibrillar material. We used cryo-ET to
379 prepare a three-dimensional surface model of the EVs, using IMOD (Mastronarde and Held
380 2017) and UCSF Chimera (Pettersen et al. 2004) to further visualize their structure and
381 fibrillar decoration (**Fig. 1F to 1H**).

382 Additional aspects of *C. neoformans* EV diversity, such as the distribution of size and
383 decoration, were analyzed. NTA analyses showed a diameter size distribution from 80 to 500
384 nm and revealed a major peak of vesicle detection in the 150-nm-diameter range (**Fig. 2A**), in
385 line with previous findings (Reis et al. 2019). We also analyzed the EV diameter frequency
386 distribution by cryo-EM from 434-single regular EV captures (**Fig. 2B**). The size distribution
387 of vesicles tracked with NTA was different from the distribution of vesicles observed with
388 cryo-EM, which revealed a wider range of EV diameter size, ranging from as small as 10 nm
389 to 500 nm (**Fig. 2C; Video S1**). Notably, smaller vesicles (< 100 nm) comprised a higher
390 proportion of vesicles captured by cryo-EM than by NTA. Although cryo-EM has some
391 statistical limitations, it nonetheless confirms the known bias of NTA towards larger EVs
392 (Bachurski et al. 2019).

393 Analysis of the EV size according to the presence or absence of the surface decoration
394 revealed a different frequency distribution (**Fig. 2D**), with non-decorated EVs showing a

395 significantly smaller size distribution ($p = 0.01$, using nonparametric Kolmogorov-Smirnov
396 test) compared to the decorated ones (**Fig. 2E**). Additionally, the analysis of the vesicular
397 decoration in 105 single regular EVs revealed heterogeneity in their thickness, ranging from 5
398 to 23 nm with the average value close to 16 nm (**Fig. 2F**). There was no correlation between
399 vesicular diameter size and decoration thickness, as indicated by linear regression analysis
400 (**Fig. 2G**). Therefore, the presence or absence of decoration, and even its thickness, does not
401 depend on the size and shape of the EVs, revealing a previously unknown aspect of fungal EV
402 diversity.

403

404 We analyzed EVs from two other pathogenic species of *Cryptococcus*, *C. deneoformans* strain JEC21 and *C. deuterogattii* strain R265. As expected, cryo-EM revealed
405 a similar structure of the EV population in the three *Cryptococcus* species, the majority of
406 EVs being decorated in *C. deneoformans* (72.4 %) and *C. deuterogattii* (81.4 %) (**Table S2**).
407 In contrast, *C. deuterogattii* EVs appeared to be smaller (median size = 48 nm) than those of
408 *C. neoformans* (median size = 67 nm) and *C. deneoformans* (median size = 70 nm) (**Fig. 3A**).
409 In addition, the thickness of decoration is smaller in *C. deneoformans* and *C. deuterogattii*
410 than in *C. neoformans* (**Fig. 3B**), suggesting a tight genetic control of these EV structural
411 properties (**Fig. 3C**, **Fig. S2**).
412

413

414 - *Cryptococcus* EVs structural analysis

415 *C. neoformans* is an encapsulated microorganism, and its capsule is mostly composed
416 of the polysaccharide glucuronoxylomannan (GXM), a critical virulence factor of this
417 pathogenic yeast (O'Meara and Alspaugh 2012). GXM has been previously shown to be
418 exported by EVs (Rodrigues et al. 2007). Therefore, we reasoned that the fibrillar decoration
419 observed around the vesicles could be composed of GXM. We thus incubated *C. neoformans*
420 EVs with the Alexa 488 labelled anti-GXM monoclonal antibody 18B7 (Casadevall et al.
421 1992), and analyzed the EV suspension by flow cytometry. More than 70% of the EVs
422 obtained from the wild-type strain were recognized by this antibody (**Fig. 4A**), suggesting that
423 most *C. neoformans* EVs are covered to some extent with GXM or derivatives thereof. While,
424 EVs obtained from the acapsular mutant strain (*cap59Δ*) (Moyrand et al. 2007) showed
425 negligible labelling (2.33%), following the same experimental approach (**Fig. 4B**).
426 Nevertheless, cryo-EM observation of *cap59Δ* EVs revealed similar fibrils as observed in the
427 wild type EVs (**Fig. 4B**). Moreover, cryo-EM analysis of EVs purified from *cap59Δ*
428 suggested a similar percentage of decorated EVs (91.6%). Overall, these data suggest that,

429 even though GXM covers most *C. neoformans* EVs, the visible fibrillar structures around
430 them are not GXM-based. Cryo-EM analysis of EVs obtained from *C. albicans* SC5314 and
431 *S. cerevisiae* S288C grown on SD medium showed a similar fibrillar decoration observed
432 around *Cryptococcus* EVs (**Fig. 4C**), reinforcing the notion that this structure is not GXM-
433 based, since neither of these two yeasts can synthesize this capsular polysaccharide.

434 We then reasoned that EV decoration could be protein-based and therefore performed
435 proteomic analyses to further explore this novel fungal vesicular feature. Two proteomic
436 analyses of *C. neoformans* EVs have been reported previously (Rodrigues et al. 2008, Wolf et
437 al. 2014) wherein the authors identified 92 and 202 proteins associated with EVs in *C.
438 neoformans*, respectively. However, neither quantitative nor enrichment of EV-associated
439 proteins was performed in these two studies. Therefore, we performed EV proteomic
440 characterization, together with an enrichment analysis in order to distinguish the proteins
441 associated with EVs, from those related to potential carry-over aggregates, inevitably
442 contaminating EV preparations.

443 In fungi, and more specifically in *Cryptococcus*, the relationship between RNA and
444 protein abundances has been reported as nearly linear, due to the relatively minor contribution
445 of posttranscriptional regulations to protein abundance (Wallace et al. 2020). We thus used
446 cellular RNA abundance at 30°C, exponential phase (Wallace et al. 2020), as a proxy for
447 cellular protein abundance, and for normalization of EV proteome data. *C. neoformans* EVs
448 proteomic analysis was performed in experimental triplicate that produced a common list
449 containing 1847 proteins (**Table S3**). Proteins were ranked according to their prevalence in
450 the sample evaluating the average intensity-based absolute quantification (IBAQ) value of the
451 three replicates. We then used the gene expression level as evaluated by RNA-seq analysis to
452 calculate an enrichment coefficient comparing the expected value in the cells with the
453 observed one in EVs. We thus identified 39 non-ribosomal proteins which were present both
454 within the 100 most prevalent EV proteins overall and the 100 most enriched proteins (**Table**
455 **S4**). We considered these proteins as EV-associated proteins. Only 9 out of these 39 proteins
456 were reported in previous proteomic analysis, emphasizing the necessity for proteomic data
457 enrichment analysis. Of note, our study and those published before used different culture
458 media, and distinct protocols of EV isolation, which might also explain the differences in
459 protein composition that were presently observed.

460 To further explore how conserved the EV protein cargo across *Cryptococcus* species
461 is, we proceeded with the same strategy to characterize the EV-associated proteins in two
462 other cryptococcal species, *C. deneoformans* (strain JEC21) and *C. deuterogattii* (strain

463 R265). We identified 38 and 48 EV-associated proteins for *C. deneoformans* and *C.*
464 *deuterogattii*, respectively (**Table S3; Table S4**). Overall, 71 EV-associated proteins were
465 identified, 37 in at least two species, and 17 shared by all the three species (**Fig. 5A and B**),
466 supporting a conserved profile of the EV-associated proteins across *Cryptococcus* species,
467 and the robustness of our analyses. Several families of proteins appeared to be typical of
468 *Cryptococcus* EVs. The major one was the Chitin deactetylase Cda family (Baker et al. 2011),
469 composed of three members present among the 17 EV-associated proteins identified in all
470 three *Cryptococcus* species analyzed. Some other families like the putative glyoxal oxidase
471 (Gox proteins), or the Ricin-type beta-trefoil lectin domain-containing protein (Ril), have one
472 member common to all three species EVs (i.e. Gox2 and Ril1) whereas the other members are
473 found in only two species (Ril2 and Ril3) or are specific of one species EVs (Gox1 and Gox3)
474 (**Fig. 5C**). We also identified three tetraspanin membrane proteins containing a SUR7/PalI
475 family motif. Tsh1 and Tsh2 shared 32% identity in their amino acid sequence. Tsh1 is
476 present in both *C. neoformans* and *C. deneoformans* EVs whilst Tsh2 was identified in both
477 *C. neoformans* and *C. deuterogattii*. The third Sur7/PalI protein shares very little sequence
478 homology beyond the SUR7 motif and is exclusive to *C. deuterogattii*. Two Sur7 proteins
479 have been recently identified in *C. albicans* EVs, suggesting that they might represent a
480 common EV marker present in fungal EVs (Dawson et al. 2020). Finally, two members of the
481 previously described pr4/barwin domain Blp protein family (Chun et al. 2011) were present in
482 *C. neoformans* and *C. deuterogattii* EVs but not in *C. deneoformans*. Similarly, the two
483 ferroxidase Cfo proteins (Jung et al. 2008) were shown to be associated only with the *C.*
484 *deuterogattii* EVs but not in the two other species.

485 Several enzymes associated with polysaccharide degradation and modifications were
486 present in *Cryptococcus* EVs. Some of these proteins are specific to one species but others are
487 present in two or all three EV proteomes. For instance, identification within the *Cryptococcus*
488 EV core proteins of Gas1 (a 1,3-beta-glucanosyltransferase), Amy1 (an alpha amylase),
489 Exg104 (a glucan 1,3-beta-glucosidase), Hep2 (a putative heparinase) together with the Gox,
490 Cda and Ril proteins suggest functions of EVs in cell wall processes, as previously
491 hypothesized in *S. cerevisiae* (Zhao et al. 2019). We also identified the BCS-inducible
492 membrane protein (Bim1), recently described as a critical factor for copper acquisition in *C.*
493 *neoformans* meningitis (Garcia-Santamarina et al. 2020). Finally, several of the EV proteins
494 identified here have no predicted function; we therefore named them Vep (Vesicles enriched
495 protein). Bioinformatics analysis of the 71 EV-associated protein sequences suggested that
496 80% might be membrane-bound, 36 of them bearing at least one putative transmembrane

497 domain as predicted by SignalP-5.0 (Almagro Armenteros et al. 2019) and/or TMHMM v. 2.0
498 (Krogh et al. 2001), and 21 being putative GPI-anchored proteins as predicted by PredGPI
499 (Pierleoni et al. 2008), which is in good agreement with putative protein-based decoration.
500 Reflecting the general specificities of these three proteomes, the GPI-anchor EV-proteomes of
501 *C. neoformans* and *C. deneoformans* are nearly identical, whereas *C. deuterogattii* is more
502 diverse (**Fig. 5D**).

503 Mature GPI-anchored proteins can also be membrane-bound and are predicted to be
504 highly mannosylated in *Cryptococcus* and other fungi (Levitz et al. 2001, de Groot et al.
505 2003). We thus reasoned that these mannosylated proteins might represent the EV decorations
506 observed by cryo-EM. To test this hypothesis, we incubated EVs with ConA conjugated to
507 Alexa Fluor 488, and further analyzed by flow cytometry. Our results demonstrated that over
508 98.5% of vesicles were recognized by this lectin, confirming the presence of mannosylated
509 proteins on the EV surface (**Fig. 6**). Similarly, EVs obtained from acapsular *cap59Δ* mutant
510 strain also showed a high percentage of staining (95.5%). Accordingly, EV treatment with
511 proteinase K was associated with a nearly complete loss of ConA labelling of both WT and
512 *cap59Δ* EVs (**Fig. 7**), overall suggesting that the outer vesicle decoration may be composed
513 primarily of mannoproteins.

514 Several genes have been implicated in protein glycosylation in *C. neoformans*. For
515 instance, *ALG3* encodes a dolichyl-phosphate-mannose-dependent α -1,3-mannosyltransferase,
516 deletion of which is associated with the production of truncated protein-associated neutral *N*-
517 glycans and a reduction in virulence (Thak et al. 2020). Similarly, *KTR3* and *HOC3* encodes
518 α 1,2-mannosyltransferase and α 1,6-mannosyltransferase, respectively, regulating *O*-glycan
519 structure and pathogenicity of *C. neoformans* (Lee et al. 2015). We reasoned that the deletion
520 of some of these genes could alter EV production and structure. We first analyzed EV
521 production in *alg3Δ*, *hoc3Δ*, and *ktr3Δ* strains by evaluating the quantity of sterol in our EV
522 preparations. We did not observe any significant alternation in EV production nor in the
523 percentage of ConA positive EVs in any of these deletion mutants (**Fig. 8A, 8B**).
524 Nevertheless, the percentage of *alg3Δ* EVs labelled by ConA was slightly reduced (**Fig. 8B**)
525 and *alg3Δ* EV decorations were less thick than wild type EVs, as revealed by cryo-EM
526 observation (**Fig. 8C, 8D; Table S2**).

527 The two most abundant *C. neoformans* EV proteins, Mp88 and Vep1/CNAG_03223
528 are GPI-anchored and represent 23.7% of the total identified proteins. Mp88 is a
529 basidiomycete specific protein originally identified as a major *C. neoformans* immunoreactive
530 mannoprotein stimulating T cell responses (Huang et al. 2002). Vep1 (Vesicles Enriched

531 Protein 1) is protein of unknown function sharing no homology with any *C. albicans* or *S.*
532 *cerevisiae* protein. In all three *Cryptococcus* species, Mp88 (Huang et al. 2002) was the most
533 prevalent EV protein. In *C. deuterogattii* EVs, in which the Vep1 protein is not present, Mp88
534 represents 35.4% of all EV proteins. We constructed the corresponding single and double
535 mutant strains for *MP88* and *VEP1* and tested their EVs for ConA binding. These mutations
536 did not strongly affect EV production although *MP88* deletion was associated with a slight
537 increased production as compared to the wild type strain (**Fig. 8A**). However, both *mp88Δ*
538 and *mp88Δ vep1Δ* EVs displayed a limited but statistically significant reduction of the ConA-
539 bound EVs as compared to EVs from wild-type strain (**Fig. 8B**). Accordingly, cryo-EM
540 analysis of *mp88Δ* EVs revealed an associated reduction of the decoration thickness (**Fig.8C**,
541 **8D**) without any change in EV size distribution (**Fig. 8C; Table S2; Fig. S2**) suggesting that
542 cryptococcal EVs might bear a highly complex decoration, probably formed from a dynamic
543 combination of mannoproteins. Combining all these data, we propose a model for cryptococcal
544 EV structure, in which, EVs are decorated by mannosylated proteins and covered by GXM
545 (**Fig. 9**).

546

547 - ***EVs for immunization and protection against cryptococcal infection***

548 Proteomic analysis of the *C. neoformans* EVs identified many immunogenic proteins,
549 including Mp88, the members of Gox and Cda families and some Vep proteins previously
550 tested as vaccine candidates against cryptococcosis (Specht et al. 2017, Hester et al. 2020).
551 Moreover, some of these proteins were also found to be enriched in *C. deneoformans* and *C.*
552 *deuterogattii* EVs (Mp88, Cda1, Cda2, Cda3, and Gox2), suggesting that secretion of these
553 immunogenic molecules via EVs could be a conserved feature across different species.
554 Taking into account that cryptococcal EVs have been shown to be immune modulators
555 (Freitas et al. 2019) and may impact the pathophysiology of the infection (Bielska et al. 2018,
556 Hai et al. 2020), we reasoned that EVs could be used for immunization against
557 cryptococcosis, avoiding the need for recombinant protein purification and adjuvant usage.
558 The usage of fungal EVs has been previously suggested as a promising vaccine strategy
559 (Vargas et al. 2015, Colombo et al. 2019, Freitas et al. 2019, Vargas et al. 2020). However, to
560 date cryptococcal EVs have not been tested in murine infection models.

561 In a pilot experiment, we obtained EVs from *C. neoformans* wild-type strain and the
562 acapsular *cap59Δ* mutant, used them to immunize BALB/c mice in two different EV-protein
563 dosages (1 and 10 µg) via intraperitoneal injections; control group was injected with only PBS
564 (four mice in each group). After three immunizations, anti-EV-antibody response was

565 evaluated in the mouse sera. Regardless of the EV origin, all the immunized mice produced
566 antibodies against vesicular proteins, as revealed by Western Blot (**Fig. 10A**). Forty days after
567 the last immunization, mice were challenged intranasally with *C. neoformans* wild type strain
568 (1×10^4 yeasts per mouse), and their survival were monitored post-infection. All EV-
569 immunized mice survived longer than the non-immunized ones and immunization with both
570 doses of *cap59 Δ* EVs statistically significantly prolonged the survival of the mice (**Fig. 10B**).
571 To note, the total carbohydrate per 100 g of EV-proteins were approximately 22 g and 3
572 g, respectively, for wild-type and *cap59 Δ* mutant, as analyzed by gas-chromatography
573 analyses (Richie et al. 2009). We then confirmed this result using a larger number of mice (10
574 mice per group). Since the highest dose of EVs from the acapsular mutant rendered the best
575 protection, we decided to proceed only with EVs from *cap59 Δ* strain (10 μ g per mouse). After
576 immunizations with EVs, the anti-EV-antibody response in the mice was analyzed; all
577 immunized mice produced antibodies against vesicular molecules (**Fig. 10C**). Following, the
578 mice were challenged with *C. neoformans* wild type strain (1×10^4 yeasts per mouse), and
579 their survival was monitored post-infection. EV-immunization led to a significant prolonged
580 survival ($p = 0.0006$) (**Fig. 10D**), thus confirming the promising potential usage of EV-based
581 protection against *Cryptococcus*.

582

583

4. Discussion

584 Studies on fungal EVs have gained much attention during recent years (Rizzo et al. 2020).
585 Although data from both pathogenic and nonpathogenic species highlight their importance in
586 diverse biological contexts, knowledge on fungal EVs is still limited, mostly due to their
587 nanometer size and the technical hurdles intrinsic to the methods applied for their
588 characterization (Rizzo et al. 2020). Here we used cutting edge technologies to revisit
589 *Cryptococcus* EVs. Our cryo-EM analysis produced an unprecedented quality of EV images
590 and resolved the fibrillar structure decoration as a new aspect on fungal EVs.

591 Our hypothesis is that EV decoration is not capsular polysaccharide GXM-based but
592 mainly composed of mannoproteins. This is supported by two independent experiments. First,
593 we demonstrated that although GXM most probably surrounds the vesicles, it is not necessary
594 for the presence of decoration. Thus, EVs produced by an acapsular strain of *C. neoformans*
595 are not bound by a GXM specific antibody yet still display decoration. Secondly, *C. albicans*
596 and *S. cerevisiae* EVs are also decorated, although none of these yeasts produced a capsular
597 polysaccharide. Nonetheless, our study revealed that the deletion of single mannoproteins,

598 such as the GPI-anchored proteins Mp88 and Vep1, was not sufficient to completely remove
599 the EV decoration, suggesting that this structure has a highly complex and dynamic
600 composition, including several mannoproteins.

601 Indeed, previous reports in *C. albicans* showed that the role of GPI-anchored proteins
602 are redundant and single mutants mostly displayed minor phenotypes, if any (Plaine et al.
603 2008). Interestingly, Johansson and coworkers performed cryo-EM analysis of *Malassezia*
604 *sympodialis* EVs, demonstrating no (Johansson et al. 2018) evident decoration on their
605 surfaces (Johansson et al. 2018). Comparative genomic analysis suggested that this lipophilic
606 pathogenic yeast, living on the skin (Theelen et al. 2018), lacks the N-glycosylation pathway
607 and possesses only a very small number of GPI-anchor proteins (Gioti et al. 2013).
608 Accordingly, *M. sympodialis* cells lack the extensive mannan outer fibrillar layer, which can
609 be easily observed at the surface of the cell wall of most yeasts including *S. cerevisiae* or *C.*
610 *albicans* (Gioti et al. 2013, Muszewska et al. 2017). Therefore, it is very tempting to
611 hypothesize that this absence of mannans in *M. sympodialis* could explain the absence of EV
612 decoration, supporting the idea that EV decoration in *Cryptococcus* species is mannoprotein-
613 based. Previous proteomic analysis of fungal EVs identified putative mannoproteins,
614 suggesting that this decoration is a common feature of fungal EVs (Bleackley et al. 2019,
615 Dawson et al. 2020, Karkowska-Kuleta et al. 2020, Rizzo et al. 2020). Accordingly, flow
616 cytometry experiments showed that *C. glabrata* EVs can be labelled by ConA (Karkowska-
617 Kuleta et al. 2020). Putative fibril-like structures have also been reported at the surface of
618 *Aspergillus fumigatus* EVs produced during cell wall regeneration (Rizzo et al. 2020).

619 In addition, we performed proteome analysis of EVs from *S. cerevisiae* and *C.*
620 *albicans* grown in the same conditions as *Cryptococcus* species, and confirmed the presence
621 of number of cell wall and GPI-anchored proteins in their EVs (Vargas et al. 2015, Zhao et al.
622 2019, Dawson et al. 2020). We also confirmed the presence of diverse antigenic proteins
623 associated with EVs in *C. albicans*, reinforcing the notion that this feature might be a general
624 aspect of pathogenic fungal EVs (**Table S5**). Whereas the presence of decoration seems to be
625 a hallmark of fungal EV, it is not specific to this kingdom (Macedo-da-Silva et al. 2021).
626 Although EVs bearing visible structures on their surface have not been commonly reported, a
627 recent cryo-EM analysis of EVs derived from human breast cell lines overexpressing
628 hyaluronan synthase 3-(HAS3) suggested the presence of fibril-like structures on their vesicle
629 surface (Noble et al. 2020). Additionally, EVs from poliovirus-infected cells contain ‘protein
630 structures with globular heads on a stalk’ around the membrane (Yang et al. 2020).

631 Nevertheless, it is still unclear how often this feature is present among the whole EV
632 population, and what the composition of these surface structures is.

633 Previous studies explored the size and morphology of fungal EVs, mostly by
634 techniques such as electron microscopy (TEM, SEM), dynamic light scattering (DLS), and
635 NTA (Albuquerque et al. 2008, Rodrigues et al. 2008, Wolf et al. 2014, Vargas et al. 2015,
636 Wolf et al. 2015, Bielska and May 2019). Here we show that cryptococcal EVs are more
637 heterogeneous than previously recognized in terms of size distribution and morphotypes. Our
638 cryo-EM analysis revealed that the peak of EV size distribution was smaller than 100 nm, and
639 substantially different from size distribution observed by NTA and from that previously found
640 from *C. neoformans* and *C. deuterogattii* EVs using NTA and DLS approaches (100 to 300
641 nm) (Reis et al. 2019). Moreover, our study revealed not only the presence of regular EVs but
642 also tubular, flat, and multilayered EVs. Although the different EV morphologies were
643 previously identified in many fungal pathogens (Albuquerque et al. 2008, Rodrigues et al.
644 2008, Tefsen et al. 2014, Vargas et al. 2015), some vesicular shapes found in this work have
645 not previously been reported. Thus, membrane tubule structures (memtubs) budding from the
646 plasma membrane were found in the arbuscular fungus *Rhizophagus irregularis*, suggesting
647 that different shapes of membranous structures could appear during fungal growth (Roth et al.
648 2019). Additionally, tubular and other morphologies were also found in EV populations
649 obtained from human biological fluids (Arraud et al. 2014, Emelyanov et al. 2020). Although
650 these data suggest that diverse structures could be part of the native EV population, the
651 cellular origins of these structures are still unknown, and we cannot rule out the possibility of
652 them being artifacts resulted from the filtration step of the commonly used EV isolation
653 protocols.

654 In this study, we demonstrated that the three *Cryptococcus* species release both
655 decorated and undecorated EVs, adding another previously unappreciated aspect to fungal EV
656 diversity. As hypothesized before, this result also suggests the existence of at least two
657 different pathways involved in EV biogenesis (Oliveira et al. 2010, Oliveira et al. 2013,
658 Bielska and May 2019, Rizzo et al. 2020). It is, therefore, reasonable to hypothesize that
659 decorated EVs could be shed from the fungal plasma membrane, “stealing” cell membrane
660 proteins when they bud out. Interestingly, the decorated EVs have larger size distribution than
661 the undecorated ones, in good agreement with what would be typical microvesicles in
662 mammals. In this hypothesis, the enrichment of tetraspanin membrane proteins containing a
663 SUR7/PalI family motif might indicate that decorated EVs could be specifically shed from the
664 Sur7 specialized plasma membrane domains. This model could be extended to other fungi as

665 Sur7 proteins have been recently identified as EV-protein markers in *C. albicans* and in the
666 wheat pathogen *Zymoseptoria tritici* (Dawson et al. 2020, Hill and Solomon 2020). This latter
667 hypothesis, together with whether or not the smaller undecorated EVs are a result of the
668 endosomal secretory pathways, thought to be exosomes being released by multivesicular
669 bodies (MVB), still needs to be further explored. Interestingly, the characterization of
670 decorated and undecorated EVs as microvesicles and exosomes, respectively, has previously
671 been proposed (Noble et al. 2020). This hypothesis and our current results are supported by a
672 recent study of *A. fumigatus* EVs in the absence of a cell wall. EVs were formed at the plasma
673 membrane level and they contained a number of plasma membrane proteins (Rizzo et al.
674 2020).

675 Our work suggests that cryptococcal EV cargo contains proteins involved in diverse
676 biological processes, including Mp88 and members of Cda and Gox families, which have
677 been suggested as immunomodulators (Specht et al. 2017, Hester et al. 2020). Since the novel
678 surface structure on fungal EVs resolved by cryo-EM resembles the spike complexes on viral
679 envelopes (Neuman et al. 2006, Zanetti et al. 2006), we reasoned they may be useful as a
680 vaccine platform. Numerous efforts are underway to develop vaccines against fungal
681 infections, although none have yet been approved for human use (Nami et al. 2019). It was
682 previously shown that the pre-treatment of *Galleria mellonella* larvae with fungal EVs
683 stimulated a protective response against a lethal challenge with *C. albicans*, *C. neoformans* or
684 *A. fumigatus* (Vargas et al. 2015, Colombo et al. 2019, Brauer et al. 2020). More recently, it
685 was also demonstrated that *C. albicans* EVs were also able to elicit a protective effect against
686 murine candidiasis (Vargas et al. 2020). Interestingly, *C. neoformans* EVs show
687 immunoreactivity with sera from patients with cryptococcosis, indicating that EV-associated
688 proteins are produced during cryptococcal infection (Rodrigues et al. 2008). Prophylactic
689 immunization is one of the effective methods to prevent cryptococcal infection, and several
690 cryptococcal antigens have been tested for their vaccination potential (Caballero Van Dyke
691 and Wormley 2018, Ueno et al. 2020). However, the *in vivo* immunoregulatory role of EVs
692 have largely remained unknown (Robbins and Morelli 2014).

693 In our study, antibody responses in cryptococcal EV-immunized mice indicate that the
694 EVs can elicit an adaptive immune response in the absence of any adjuvants or carriers,
695 unlike other antigenic proteins of *Cryptococcus* (Specht et al. 2017). It is also important to
696 note that immunization using *C. neoformans* heat-killed cells does not elicit protection in a
697 murine model of infection (Masso-Silva et al. 2018). EV-based vaccination data obtained by
698 other groups using an invertebrate model suggest that innate immunity might also be involved

699 (Vargas et al. 2015, Colombo et al. 2019). As *Cryptococcus* predominantly infects
700 immunocompromised hosts, it will be worth checking the role of EVs in eliciting trained
701 immunity, wherein innate immune cells develop memory-like response against an antigen
702 upon repeated exposure (Hole et al. 2019, Mulder et al. 2019). The mechanisms, and the
703 responsible immune cell types leading to prolonged survival in our murine infection model,
704 remain to be deciphered. Although EV immunization was not sufficient to prevent death, we
705 believe that adjusting the antigens exposed on EV surface could potentially increase the
706 protective effect. In that sense, the fact that EVs from *C. neoformans* WT and the acapsular
707 mutant did not lead to the same level of protection is an encouraging data.

708 Overall, the fantastic power of cryo-EM, together with several innovative analyses,
709 has enabled us to draw a new model of fungal EVs and revealed new aspects of their
710 diversity, suggesting different biosynthetic pathways. This model supports new strategies to
711 construct vaccines against these too often neglected infectious diseases. It also opens the door
712 to more questions concerning the origin and the fate of fungal EVs.

713

714

715 5. References

716

717 Albuquerque PC, Nakayasu ES, Rodrigues ML, Frases S, Casadevall A, Zancope-Oliveira RM, Almeida
718 IC, Nosanchuk JD 2008. Vesicular transport in *Histoplasma capsulatum*: an effective mechanism for
719 trans-cell wall transfer of proteins and lipids in ascomycetes. *Cell Microbiol* 10: 1695-1710.

720 Almagro Armenteros JJ, Tsirigos KD, Sønderby CK, Petersen TN, Winther O, Brunak S, von Heijne G,
721 Nielsen H 2019. SignalP 5.0 improves signal peptide predictions using deep neural networks. *Nature
722 Biotechnol* 37: 420-423.

723 Arraud N, Linares R, Tan S, Gounou C, Pasquet JM, Mornet S, Brisson AR 2014. Extracellular vesicles
724 from blood plasma: determination of their morphology, size, phenotype and concentration. *Journal
725 of Thrombosis and Haemostasis* 12: 614-627.

726 Bachurski D, Schuldner M, Nguyen P-H, Malz A, Reiners KS, Grenzi PC, Babatz F, Schauss AC, Hansen
727 HP, et al. 2019. Extracellular vesicle measurements with nanoparticle tracking analysis - An accuracy
728 and repeatability comparison between NanoSight NS300 and ZetaView. *J Extracell Vesicles* 8:
729 1596016-1596016.

730 Baker LG, Specht CA, Lodge JK 2011. Cell Wall Chitosan Is Necessary for Virulence in the
731 Opportunistic Pathogen *Cryptococcus neoformans*. *Eukaryot Cell* 10: 1264.

732 Bielska E, May RC 2019. Extracellular vesicles of human pathogenic fungi. *Curr Opinion Microbiol* 52:
733 90-99.

734 Bielska E, Sisquella MA, Aldeieg M, Birch C, O'Donoghue EJ, May RC 2018. Pathogen-derived
735 extracellular vesicles mediate virulence in the fatal human pathogen *Cryptococcus gattii*. *Nature Com*
736 9: 1556-1556.

737 Bleackley MR, Dawson CS, Anderson MA 2019. Fungal extracellular vesicles with a focus on
738 proteomic analysis. *PROTEOMICS* 19: 1800232.

739 Bleackley MR, Samuel M, Garcia-Ceron D, McKenna JA, Lowe RGT, Pathan M, Zhao K, Ang C-S,
740 Mathivanan S, et al. 2020. Extracellular Vesicles From the Cotton Pathogen *Fusarium oxysporum* f.
741 sp. *vasinfectum* Induce a Phytotoxic Response in Plants. *Frontiers in plant science* 10: 1610-1610.

742 Brauer VS, Pessoni AM, Bitencourt TA, de Paula RG, de Oliveira Rocha L, Goldman GH, Almeida F
743 2020. Extracellular vesicles from *Aspergillus flavus* induce M1 polarization *in vitro*. *mSphere* 5:
744 e00190-00120.

745 Caballero Van Dyke MC, Wormley FL, Jr. 2018. A Call to Arms: Quest for a Cryptococcal Vaccine.
746 *Trends Microbiol* 26: 436-446.

747 Casadevall A, Mukherjee J, Devi SJN, Schneerson R, Robbins JB, Scharff MD 1992. Antibodies elicited
748 by a *Cryptococcus neoformans*-tetanus toxoid conjugate vaccine have the same specificity as those
749 elicited in infection. *The Journal of Infectious Diseases* 165: 1086-1093.

750 Chiang C-Y, Chen C 2019. Toward characterizing extracellular vesicles at a single-particle level. *J
751 Biomed Sci* 26: 9-9.

752 Chiou N-T, Kageyama R, Ansel KM 2018. Selective Export into Extracellular Vesicles and Function of
753 tRNA Fragments during T Cell Activation. *Cell Rep.* 25: 3356-3370.e3354.

754 Chun CD, Brown JCS, Madhani HD 2011. A major role for capsule-independent phagocytosis-
755 inhibitory mechanisms in mammalian infection by *Cryptococcus neoformans*. *Cell host & microbe* 9:
756 243-251.

757 Coakley G, McCaskill JL, Borger JG, Simbiri F, Robertson E, Millar M, Harcus Y, McSorley HJ, Maizels
758 RM, et al. 2017. Extracellular Vesicles from a Helminth Parasite Suppress Macrophage Activation and
759 Constitute an Effective Vaccine for Protective Immunity. *Cell Rep.* 19: 1545-1557.

760 Collopy PD, Colot HV, Park G, Ringelberg C, Crew CM, Borkovich KA, Dunlap JC 2010. High-throughput
761 construction of gene deletion cassettes for generation of *Neurospora crassa* knockout strains.
762 *Methods Mol Biol* 638: 33-40.

763 Colombo AC, Rella A, Normile T, Joffe LS, Tavares PM, de S. Araújo GR, Frases S, Orner EP, Farnoud
764 AM, et al. 2019. *Cryptococcus neoformans* glucuronoxylomannan and sterolglucoside are required for
765 host protection in an animal vaccination model. *mBio* 10: e02909-02918.

766 Cox J, Mann M 2008. MaxQuant enables high peptide identification rates, individualized p.p.b.-range
767 mass accuracies and proteome-wide protein quantification. *Nature Biotechnol* 26: 1367-1372.

768 Cox J, Neuhauser N, Michalski A, Scheltema RA, Olsen JV, Mann M 2011. Andromeda: A Peptide
769 Search Engine Integrated into the MaxQuant Environment. *Journal of Proteome Research* 10: 1794-
770 1805.

771 da Silva RP, Puccia R, Rodrigues ML, Oliveira DL, Joffe LS, César GV, Nimrichter L, Goldenberg S, Alves
772 LR 2015. Extracellular vesicle-mediated export of fungal RNA. *Sci Rep* 5: 7763.

773 Dawson CS, Garcia-Ceron D, Rajapaksha H, Faou P, Bleackley MR, Anderson MA 2020. Protein
774 markers for *Candida albicans* EVs include claudin-like Sur7 family proteins. *J Extracell Vesicles* 9:
775 1750810.

776 de Groot PWJ, Hellingwerf KJ, Klis FM 2003. Genome-wide identification of fungal GPI proteins. *Yeast*
777 20: 781-796.

778 Deatherage BL, Cookson BT 2012. Membrane Vesicle Release in Bacteria, Eukaryotes, and Archaea: a
779 Conserved yet Underappreciated Aspect of Microbial Life. *Infect Immun* 80: 1948.

780 Eisenman HC, Frases S, Nicola AM, Rodrigues ML, Casadevall A 2009. Vesicle-associated melanization
781 in *Cryptococcus neoformans*. *Microbiology* 155: 3860-3867.

782 Emelyanov A, Shtam T, Kamyshinsky R, Garaeva L, Verlov N, Miliukhina I, Kudrevatykh A, Gavrilov G,
783 Zabrodskaya Y, et al. 2020. Cryo-electron microscopy of extracellular vesicles from cerebrospinal
784 fluid. *PLOS ONE* 15: e0227949.

785 Fan Y, Lin X 2018. Multiple Applications of a Transient CRISPR-Cas9 Coupled with Electroporation
786 (TRACE) System in the *Cryptococcus neoformans* Species Complex. *Genetics* 208: 1357.

787 Freitas MS, Bonato VLD, Pessoni AM, Rodrigues ML, Casadevall A, Almeida F 2019. Fungal
788 Extracellular Vesicles as Potential Targets for Immune Interventions. *mSphere* 4: e00747-00719.

789 Garcia-Santamarina S, Probst C, Festa RA, Ding C, Smith AD, Conklin SE, Brander S, Kinch LN, Grishin
790 NV, et al. 2020. A lytic polysaccharide monooxygenase-like protein functions in fungal copper import
791 and meningitis. *Nat Chem Biol* 16: 337-344.

792 Gioti A, Nystedt B, Li W, Xu J, Andersson A, Averette AF, Münch K, Wang X, Kappauf C, et al. 2013.
793 Genomic Insights into the Atopic Eczema-Associated Skin Commensal Yeast Malassezia
794 sympodialis. *mBio* 4: e00572-00512.

795 Gonzalez-Hilarion S, Paulet D, Lee K-T, Hon C-C, Lechat P, Mogensen E, Moyrand F, Proux C, Barboux
796 R, et al. 2016. Intron retention-dependent gene regulation in *Cryptococcus neoformans*. *Sci Rep* 6:
797 32252.

798 Gröhs Ferrareze PA, Maufrais C, Silva Araujo Streit R, Priest SJ, Cuomo CA, Heitman J, Staats CC,
799 Janbon G 2021. Application of an optimized annotation pipeline to the *Cryptococcus deuterogattii*
800 genome reveals dynamic primary metabolic gene clusters and genomic impact of RNAi loss. *G3*
801 (Bethesda) 11.

802 Hagen F, Khayhan K, Theelen B, Kolecka A, Polacheck I, Sionov E, Falk R, Parnmen S, Lumbsch HT, et
803 al. 2015. Recognition of seven species in the *Cryptococcus gattii*/*Cryptococcus neoformans* species
804 complex. *Fungal Genet Biol* 78: 16-48.

805 Hai TP, Tuan TL, Van Anh D, Mai TN, Phu Huong LN, Thwaites GE, Johnson E, Van Vinh Chau N, Ashton
806 P, et al. 2020. The expression of virulence by the *Cryptococcus neoformans* VNla-5 lineage is plastic
807 and associated with host immune background. *bioRxiv*: 2020.2002.2024.962134.

808 Hester MM, Lee CK, Abraham A, Khoshkenar P, Ostroff GR, Levitz SM, Specht CA 2020. Protection of
809 mice against experimental cryptococcosis using glucan particle-based vaccines containing novel
810 recombinant antigens. *Vaccine* 38: 620-626.

811 Hill E, Solomon P (2020). Extracellular Vesicles from the Apoplastic Fungal Wheat Pathogen
812 *Zymoseptoria tritici*, Research Square.

813 Hole CR, Wager CML, Castro-Lopez N, Campuzano A, Cai H, Wozniak KL, Wang Y, Wormley FL 2019.
814 Induction of memory-like dendritic cell responses in vivo. *Nature Com* 10: 2955.

815 Huang C, Nong SH, Mansour MK, Specht CA, Levitz SM 2002. Purification and characterization of a
816 second immunoreactive mannoprotein from *Cryptococcus neoformans* that stimulates T-cell
817 responses. *Infect Immun* 70: 5485-5493.

818 Janbon G, Ormerod KL, Paulet D, Byrnes III EJ, Chatterjee G, Yadav V, Mullapudi N, Hon CC, Billmyre
819 RB, et al. 2014. Analysis of the genome and transcriptome of *Cryptococcus neoformans* var. *grubii*
820 reveals complex RNA expression and microevolution leading to virulence attenuation. *PLoS Genet* 10:
821 e1004261.

822 Janbon G, Quintin J, Lanterrier F, d'Enfert C 2019. Studying fungal pathogens of humans and fungal
823 infections: fungal diversity and diversity of approaches. *Genes Immun* 20: 403-414.

824 Joffe LS, Nimrichter L, Rodrigues ML, Del Poeta M 2016. Potential Roles of Fungal Extracellular
825 Vesicles during Infection. *mSphere* 1: e00099-00016.

826 Johansson HJ, Vallhov H, Holm T, Gehrmann U, Andersson A, Johansson C, Blom H, Carroni M, Lehtio
827 J, et al. 2018. Extracellular nanovesicles released from the commensal yeast *Malassezia sympodialis*
828 are enriched in allergens and interact with cells in human skin. *Sci Rep* 8: 9182.

829 Jung WH, Sham A, Lian T, Singh A, Kosman DJ, Kronstad JW 2008. Iron source preference and
830 regulation of iron uptake in *Cryptococcus neoformans*. *PLoS Pathog* 4: e45.

831 Karkowska-Kuleta J, Kulig K, Karnas E, Zuba-Surma E, Woznicka O, Pyza E, Kuleta P, Osyczka A, Rapala-
832 Kozik M, et al. 2020. Characteristics of extracellular vesicles released by the pathogenic yeast-like
833 fungi *Candida glabrata*, *Candida parapsilosis* and *Candida tropicalis*. *Cells* 9: 1722.

834 Kremer JR, Mastronarde DN, McIntosh JR 1996. Computer Visualization of Three-Dimensional Image
835 Data Using IMOD. *Journal of Structural Biology* 116: 71-76.

836 Krogh A, Larsson B, von Heijne G, Sonnhammer ELL 2001. Predicting transmembrane protein
837 topology with a hidden markov model: application to complete genomes. *J Mol Biol* 305: 567-580.

838 Kwon-Chung KJ, Fraser JA, Doering TL, Wang Z, Janbon G, Idnurm A, Bahn YS 2014. *Cryptococcus*
839 *neoformans* and *Cryptococcus gattii*, the etiologic agents of cryptococcosis. *Cold Spring Harb Perspect*
840 *Med* 4: a019760.

841 Lee DJ, Bahn YS, Kim HJ, Chung SY, Kang HA 2015. Unraveling the novel structure and biosynthetic
842 pathway of O-linked glycans in the Golgi apparatus of the human pathogenic yeast *Cryptococcus*
843 *neoformans*. *J Biol Chem* 290: 1861-1873.

844 Leone F, Bellani L, Muccifora S, Giorgetti L, Bongioanni P, Simili M, Maserti B, Del Carratore R 2018.
845 Analysis of extracellular vesicles produced in the biofilm by the dimorphic yeast *Pichia fermentans*.
846 *Journal of Cellular Physiology* 233: 2759-2767.

847 Levitz SM, Nong S, Mansour MK, Huang C, Specht CA 2001. Molecular characterization of a
848 mannoprotein with homology to chitin deacetylases that stimulates T cell responses to *Cryptococcus*
849 *neoformans*. *Proc Natl Acad Sci USA* 98: 10422-10427.

850 Maas SLN, de Vrij J, van der Vlist EJ, Geragousian B, van Bloois L, Mastrobattista E, Schiffelers RM,
851 Wauben MHM, Broekman MLD, et al. 2015. Possibilities and limitations of current technologies for
852 quantification of biological extracellular vesicles and synthetic mimics. *Journal of Controlled Release*
853 200: 87-96.

854 Macedo-da-Silva J, Santiago VF, Rosa-Fernandes L, Marinho CRF, Palmisano G 2021. Protein
855 glycosylation in extracellular vesicles: Structural characterization and biological functions. *Mol*
856 *Immunol* 135: 226-246.

857 Masso-Silva J, Espinosa V, Liu T-B, Wang Y, Xue C, Rivera A 2018. The F-Box protein Fbp1 shapes the
858 immunogenic potential of *Cryptococcus neoformans*. *mBio* 9: e01828-01817.

859 Mastronarde DN 2005. Automated electron microscope tomography using robust prediction of
860 specimen movements. *Journal of Structural Biology* 152: 36-51.

861 Mastronarde DN, Held SR 2017. Automated tilt series alignment and tomographic reconstruction in
862 IMOD. *Journal of structural biology* 197: 102-113.

863 Meldolesi J 2018. Exosomes and Ectosomes in Intercellular Communication. *Curr Biol* 28: R435-R444.

864 Moyrand F, Fontaine T, Janbon G 2007. Systematic capsule gene disruption reveals the central role of
865 galactose metabolism on *Cryptococcus neoformans* virulence. *Mol Microbiol* 64: 771-781.

866 Mulder WJM, Ochando J, Joosten LAB, Fayad ZA, Netea MG 2019. Therapeutic targeting of trained
867 immunity. *Nat Rev Drug Discov* 18: 553-566.

868 Muszewska A, Piłsyk S, Perlińska-Lenart U, Kruszewska JS 2017. Diversity of Cell Wall Related Proteins
869 in Human Pathogenic Fungi. *Journal of fungi (Basel, Switzerland)* 4: 6.

870 Nami S, Mohammadi R, Vakili M, Khezripour K, Mirzaei H, Morovati H 2019. Fungal vaccines,
871 mechanism of actions and immunology: A comprehensive review. *Biomedicine & Pharmacotherapy*
872 109: 333-344.

873 Neuman BW, Adair BD, Yoshioka C, Quispe JD, Orca G, Kuhn P, Milligan RA, Yeager M, Buchmeier MJ
874 2006. Supramolecular architecture of severe acute respiratory syndrome coronavirus revealed by
875 electron cryomicroscopy. *J Virol* 80: 7918-7928.

876 Noble JM, Roberts LM, Vidavsky N, Chiou AE, Fischbach C, Paszek MJ, Estroff LA, Kourkoutis LF 2020.
877 Direct comparison of optical and electron microscopy methods for structural characterization of
878 extracellular vesicles. *Journal of Structural Biology* 210: 107474.

879 O'Meara TR, Alspaugh JA 2012. The *Cryptococcus neoformans* capsule: a sword and a shield. *Clin
880 Microbiol Rev* 25: 387-408.

881 Oliveira DL, Freire-de-Lima CG, Nosanchuk JD, Casadevall A, Rodrigues ML, Nimrichter L 2010.
882 Extracellular vesicles from *Cryptococcus neoformans* modulate macrophage functions. *Infect Immun*
883 78: 1601-1609.

884 Oliveira DL, Nakayasu ES, Joffe LS, Guimarães AJ, Sobreira TJP, Nosanchuk JD, Cordero RJB, Frases S,
885 Casadevall A, et al. 2010. Characterization of Yeast Extracellular Vesicles: Evidence for the
886 Participation of Different Pathways of Cellular Traffic in Vesicle Biogenesis. *PLOS ONE* 5: e11113.

887 Oliveira DL, Nimrichter L, Miranda K, Frases S, Faull KF, Casadevall A, Rodrigues ML 2009.
888 *Cryptococcus neoformans* cryoultramicrotomy and vesicle fractionation reveals an intimate
889 association between membrane lipids and glucuronoxylosemannan. *Fungal Genet Biol* 46: 956-963.

890 Oliveira DL, Rizzo J, Joffe LS, Godinho RMC, Rodrigues ML 2013. Where do they come from and
891 where do they go: candidates for regulating extracellular vesicle formation in fungi. *Int J Mol Sci* 14:
892 9581-9603.

893 Orlov I, Myasnikov AG, Andronov L, Natchiar SK, Khatter H, Beinsteiner B, Ménétret J-F, Hazemann I,
894 Mohideen K, et al. 2017. The integrative role of cryo electron microscopy in molecular and cellular
895 structural biology. *Biology of the Cell* 109: 81-93.

896 Pettersen EF, Goddard TD, Huang CC, Couch GS, Greenblatt DM, Meng EC, Ferrin TE 2004. UCSF
897 Chimera—A visualization system for exploratory research and analysis. *Journal of Computational
898 Chemistry* 25: 1605-1612.

899 Pierleoni A, Martelli PL, Casadio R 2008. PredGPI: a GPI-anchor predictor. *BMC Bioinformatics* 9: 392.

900 Plaine A, Walker L, Da Costa G, Mora-Montes HM, McKinnon A, Gow NAR, Gaillardin C, Munro CA,
901 Richard ML 2008. Functional analysis of *Candida albicans* GPI-anchored proteins: roles in cell wall
902 integrity and caspofungin sensitivity. *Fungal genetics and biology : FG & B* 45: 1404-1414.

903 Rajasingham R, Smith RM, Park BJ, Jarvis JN, Govender NP, Chiller TM, Denning DW, Loyse A,
904 Boulware DR 2017. Global burden of disease of HIV-associated cryptococcal meningitis: an updated
905 analysis. *The Lancet Infectious Diseases* 17: 873-881.

906 Rayner S, Bruhn S, Vallhov H, Andersson A, Billmyre RB, Scheynius A 2017. Identification of small
907 RNAs in extracellular vesicles from the commensal yeast *Malassezia sympodialis*. *Sci Rep* 7: 39742.

908 Reis FCG, Borges BS, Jozefowicz LJ, Sena BAG, Garcia AWA, Medeiros LC, Martins ST, Honorato L,
909 Schrank A, et al. 2019. A Novel Protocol for the Isolation of Fungal Extracellular Vesicles Reveals the
910 Participation of a Putative Scramblase in Polysaccharide Export and Capsule Construction in
911 *Cryptococcus gattii*. *mSphere* 4: e00080-00019.

912 Reis FCG, Costa JH, Honorato L, Nimrichter L, Fill TP, Rodrigues ML 2021. Small Molecule Analysis of
913 Extracellular Vesicles Produced by *Cryptococcus gattii*: Identification of a Tripeptide Controlling
914 Cryptococcal Infection in an Invertebrate Host Model. *Front Immunol* 12.

915 Richie DL, Hartl L, Aimanianda V, Winters MS, Fuller KK, Miley MD, White S, McCarthy JW, Latgé J-P,
916 et al. 2009. A role for the unfolded protein response (UPR) in virulence and antifungal susceptibility
917 in *Aspergillus fumigatus*. *PLoS Pathog* 5: e1000258-e1000258.

918 Rizzo J, Albuquerque PC, Wolf JM, Nascimento R, Pereira MD, Nosanchuk JD, Rodrigues ML 2017. Analysis of multiple components involved in the interaction between *Cryptococcus neoformans* and 919 *Acanthamoeba castellanii*. *Fungal Biology* 121: 602-614.

920 Rizzo J, Chaze T, Miranda K, Roberson RW, Gorgette O, Nimrichter L, Matondo M, Latgé J-P, Beauvais 921 A, et al. 2020. Characterization of extracellular vesicles produced by *Aspergillus fumigatus* 922 protoplasts. *mSphere* 5: e00476-00420.

923 Rizzo J, Rodrigues ML, Janbon G 2020. Extracellular Vesicles in Fungi: Past, Present, and Future 924 Perspectives. *Front Cell Infect Microbiol* 10.

925 Robbins PD, Morelli AE 2014. Regulation of immune responses by extracellular vesicles. *Nat Rev Immunol* 14: 195-208.

926 Rodrigues ML, Casadevall A 2018. A two-way road: novel roles for fungal extracellular vesicles. *Mol Microbiol* 110: 11-15.

927 Rodrigues ML, Godinho RMC, Zamith-Miranda D, Nimrichter L 2015. Traveling into Outer Space: 928 Unanswered Questions about Fungal Extracellular Vesicles. *PLoS Pathog* 11: e1005240.

929 Rodrigues ML, Nakayasu ES, Oliveira DL, Nimrichter L, Nosanchuk JD, Almeida IC, A. C 2008. 930 Extracellular vesicles produced by *Cryptococcus neoformans* contain protein components associated 931 with virulence. *Eukaryot Cell* 7: 58-67.

932 Rodrigues ML, Nimrichter L, Oliveira DL, Frases S, Miranda K, Zaragoza O, Alvarez M, Nakouzi A, 933 Feldmesser M, et al. 2007. Vesicular polysaccharide export in *Cryptococcus neoformans* is a 934 eukaryotic solution to the problem of fungal trans-cell wall transport. *Eukaryot Cell* 6: 48-59.

935 Roth R, Hillmer S, Funaya C, Chiapello M, Schumacher K, Lo Presti L, Kahmann R, Paszkowski U 2019. 936 Arbuscular cell invasion coincides with extracellular vesicles and membrane tubules. *Nature Plants* 5: 937 204-211.

938 Schorb M, Haberbosch I, Hagen WJH, Schwab Y, Mastronarde DN 2019. Software tools for automated 939 transmission electron microscopy. *Nature Meth* 16: 471-477.

940 Schwanhäusser B, Busse D, Li N, Dittmar G, Schuchhardt J, Wolf J, Chen W, Selbach M 2011. Global 941 quantification of mammalian gene expression control. *Nature* 473: 337-342.

942 Shopova IA, Belyaev I, Dasari P, Jahreis S, Stroe MC, Cseresnyés Z, Zimmermann A-K, Medyukhina A, 943 Svensson C-M, et al. 2020. Human Neutrophils Produce Antifungal Extracellular Vesicles against 944 *Aspergillus fumigatus*. *mBio* 11: e00596-00520.

945 Souza JAM, Baltazar LdM, Carregal VM, Gouveia-Eufrasio L, de Oliveira AG, Dias WG, Campos Rocha 946 M, Rocha de Miranda K, Malavazi I, et al. 2019. Characterization of *Aspergillus fumigatus* 947 extracellular vesicles and their effects on macrophages and neutrophils functions. *Front Microbiol* 10: 948 2008-2008.

949 Specht CA, Lee CK, Huang H, Hester MM, Liu J, Luckie BA, Torres Santana MA, Mirza Z, Khoshkenar P, 950 et al. 2017. Vaccination with Recombinant *Cryptococcus* Proteins in Glucan Particles Protects Mice 951 against Cryptococcosis in a Manner Dependent upon Mouse Strain and Cryptococcal Species. *mBio* 8: 952 e01872-01817.

953 Tefsen B, Grijpstra J, Ordonez S, Lammers M, van Die I, de Cock H 2014. Deletion of the CAP10 gene 954 of *Cryptococcus neoformans* results in a pleiotropic phenotype with changes in expression of 955 virulence factors. *Research in Microbiology* 165: 399-410.

956 Thak EJ, Lee S-B, Xu-Vanpala S, Lee D-J, Chung S-Y, Bahn Y-S, Oh D-B, Shinohara ML, Kang HA 2020. 957 Core N-glycan structures are critical for the pathogenicity of *Cryptococcus neoformans* by modulating 958 host cell death. *mBio* 11: e00711-00720.

959 Theelen B, Cafarchia C, Gaitanis G, Bassukas ID, Boekhout T, Dawson TL, Jr. 2018. Malassezia ecology, 960 pathophysiology, and treatment. *Med Mycol* 56: S10-S25.

961 Théry C, Witwer KW, Aikawa E, Alcaraz MJ, Anderson JD, Andriantsitohaina R, Antoniou A, Arab T, 962 Archer F, et al. 2018. Minimal information for studies of extracellular vesicles 2018 (MISEV2018): a 963 position statement of the International Society for Extracellular Vesicles and update of the 964 MISEV2014 guidelines. *J Extracell Vesicles* 7: 1535750-1535750.

965 Tyanova S, Temu T, Cox J 2016. The MaxQuant computational platform for mass spectrometry-based 966 shotgun proteomics. *Nature Protocols* 11: 2301-2319.

967

970 Ueno K, Yanagihara N, Shimizu K, Miyazaki Y 2020. Vaccines and protective immune memory
971 against Cryptococcosis. *Biol. Pharm. Bull.* 43.

972 Vallejo MC, Nakayasu ES, Longo LVG, Ganiko L, Lopes FG, Matsuo AL, Almeida IC, Puccia R 2012.
973 Lipidomic analysis of extracellular vesicles from the pathogenic phase of *Paracoccidioides brasiliensis*.
974 *PLoS one* 7: e39463-e39463.

975 Van Der Pol E, Hoekstra AG, Sturk A, Otto C, Van Leeuwen TG, Nieuwland R 2010. Optical and non-
976 optical methods for detection and characterization of microparticles and exosomes. *Journal of*
977 *Thrombosis and Haemostasis* 8: 2596-2607.

978 van Niel G, D'Angelo G, Raposo G 2018. Shedding light on the cell biology of extracellular vesicles.
979 *Nature Reviews Molecular Cell Biology* 19: 213-228.

980 Vargas G, Honorato L, Guimarães AJ, Rodrigues ML, Reis FCG, Vale AM, Ray A, Nosanchuk JD,
981 Nimrichter L 2020. Protective effect of fungal extracellular vesicles against murine candidiasis. *Cell*
982 *Microbiol* n/a: e13238.

983 Vargas G, Rocha JDB, Oliveira DL, Albuquerque PC, Frases S, Santos SS, Nosanchuk JD, Gomes AMO,
984 Medeiros LCAS, et al. 2015. Compositional and immunobiological analyses of extracellular vesicles
985 released by *Candida albicans*. *Cell Microbiol* 17: 389-407.

986 Wallace EWJ, Maufrais C, Sales-Lee J, Tuck LR, de Oliveira L, Feuerbach F, Moyrand F, Natarajan P,
987 Madhani HD, et al. 2020. Quantitative global studies reveal differential translational control by start
988 codon context across the fungal kingdom. *Nucleic Acids Res* 48: 2312-2331.

989 Wang X, Thompson CD, Weidenmaier C, Lee JC 2018. Release of *Staphylococcus aureus* extracellular
990 vesicles and their application as a vaccine platform. *Nature Com* 9: 1379-1379.

991 Witwer KW, Théry C 2019. Extracellular vesicles or exosomes? On primacy, precision, and popularity
992 influencing a choice of nomenclature. *J Extracell Vesicles* 8: 1648167.

993 Wolf JM, Espadas-Moreno J, Luque-Garcia JL, Casadevall A 2014. Interaction of *Cryptococcus*
994 *neoformans* extracellular vesicles with the cell wall. *Eukaryot Cell* 13: 1484-1493.

995 Wolf JM, Espadas J, Luque-Garcia J, Reynolds T, Casadevall A 2015. Lipid biosynthetic genes affect
996 *Candida albicans* extracellular vesicle morphology, cargo, and immunostimulatory properties.
997 *Eukaryot Cell* 14: 745-754.

998 Xu R, Rai A, Chen M, Suwakulsiri W, Greening DW, Simpson RJ 2018. Extracellular vesicles in cancer
999 — implications for future improvements in cancer care. *Nature Reviews Clinical Oncology* 15: 617-
1000 638.

1001 Yang B, Wang J, Jiang H, Lin H, Ou Z, Ullah A, Hua Y, Chen J, Lin X, et al. 2021. Extracellular vesicles
1002 derived from *Talaromyces marneffei* yeasts mediate inflammatory response in macrophage cells by
1003 bioactive protein components. *Front Microbiol* 11.

1004 Yang JE, Rossignol ED, Chang D, Zaia J, Forrester I, Raja K, Winbigler H, Nicastro D, Jackson WT, et al.
1005 2020. Complexity and ultrastructure of infectious extracellular vesicles from cells infected by non-
1006 enveloped virus. *Sci Rep* 10: 7939.

1007 Zabeo D, Cvjetkovic A, Lässer C, Schorb M, Lötvall J, Höög JL 2017. Exosomes purified from a single
1008 cell type have diverse morphology. *J Extracell Vesicles* 6: 1329476-1329476.

1009 Zanetti G, Briggs JAG, Grünewald K, Sattentau QJ, Fuller SD 2006. Cryo-Electron Tomographic
1010 Structure of an Immunodeficiency Virus Envelope Complex In Situ. *PLoS Pathog* 2: e83.

1011 Zarnowski R, Sanchez H, Covelli AS, Dominguez E, Jaromin A, Bernhardt J, Mitchell KF, Heiss C, Azadi
1012 P, et al. 2018. *Candida albicans* biofilm-induced vesicles confer drug resistance through matrix
1013 biogenesis. *PLoS Biol* 16: e2006872.

1014 Zhao K, Bleackley M, Chisanga D, Gangoda L, Fonseka P, Liem M, Kalra H, Al Saffar H, Keerthikumar S,
1015 et al. 2019. Extracellular vesicles secreted by *Saccharomyces cerevisiae* are involved in cell wall
1016 remodelling. *Communications Biology* 2: 305.

1017
1018

1019 **Geolocalisation**

1020	Juliana RIZZO	ORCID	0000-0001-5538-6471
1021	Sarah Sze Wah WONG	ORCID	0000-0002-9440-1774
1022	Anastasia D. GAZI	ORCID	0000-0002-2922-3625
1023	Thibault CHAZE	ORCID	0000-0002-3615-7021
1024	Pierre-Henri COMMERE	ORCID	0000-0002-3886-4256
1025	Sophie NOVAULT	ORCID	0000-0001-5708-3597
1026	Mariette MATONDO	ORCID	0000-0003-3958-7710
1027	Gerard PEHAUD-ARNAUDET	ORCID	0000-0001-6479-9470
1028	Lysangela R ALVES	ORCID	0000-0002-1972-2658
1029	Robin C. MAY	ORCID	0000-0001-5364-1838
1030	Leonardo NIMRICHTER	ORCID	0000-0001-9281-6856
1031	Marcio L. RODRIGUES :	ORCID	0000-0002-6081-3439
1032	Vishukumar AIMANIANDA :	ORCID	0000-0001-5813-7497
1033	Guilhem JANBON :	ORCID	0000-0002-4788-1154

1034

1035

1036

1037 **Acknowledgements**

1038

1039 This work was supported by a CAPES COFECUB grant n°39712ZK (to GJ, MLR, LA and
1040 LN). JR was supported by the CAPES-COFECUB Franco-Brazilian Research Exchange
1041 Program (88887.357947/2019-00) and by a Pasteur-Roux-Cantarini fellowship of Institut
1042 Pasteur. SSWW was supported by CEFIPRA/ANR-DFG-AfuINF grant and Pasteur-Roux-
1043 Cantarini postdoctoral fellowship. VA was supported by ANR-DFG AfuINF and Indo-French
1044 Centre for the Promotion of Advanced Research (CEFIPRA; Grant N°5403-1) grants. Jean-
1045 Marie Winter from the NanoImaging Core at Institut Pasteur is acknowledged for his support
1046 image acquisition. The NanoImaging Core was created with the help of a grant from the
1047 French Government's 'Investissements d'Avenir' program (EQUIPEX CACSICE – "Centre
1048 d'analyse de systèmes complexes dans les environnements complexes", ANR-11-EQPX-
1049 0008). The Falcon II equipping the F20 microscope at the UBI used during this study was also
1050 financed by the Equipex CACSICE (grant number ANR-11-EQPX-0008). M.L.R. is
1051 supported by grants from the Brazilian Ministry of Health (grant 440015/2018-9), Conselho
1052 Nacional de Desenvolvimento Científico e Tecnológico (CNPq; grants 405520/2018-2 and
1053 301304/2017-3), and Fiocruz (grants VPPCB-007-FIO-18 and VPPIS-001-FIO18)MLR, JR,
1054 and FCGR also acknowledge support from Coordenac^{ão} de Aperfeic^{amento} de Pessoal
1055 de Nível Superior (CAPES, finance code 001) and the Instituto Nacional de Ci^{encia} e
1056 Tecnologia de Inova^{cão} em Doenc^{as} de Populac^{ões} Negligenciadas (INCT-IDPN).
1057 MLR is currently on leave of an associate professor position at the Instituto de Microbiologia

1058 Paulo de Góes of the Universidade Federal do Rio de Janeiro. We thank Adèle Trottier for her
1059 help in the preparation of EV samples.

1060

1061

1062 **Figures legends**

1063

1064 **Figure 1: Cryo-electron microscopy analysis of *C. neoformans* extracellular vesicles**
1065 **(EVs).**

1066 Cryo-EM analysis revealed a heterogeneous population of vesicles with diverse structural
1067 aspects, previously unappreciated in fungal EVs (A). As shown, the EVs were delimitated by
1068 a lipid bilayer (B to E), which showed either no decoration (in 10.8% vesicles, panels B and
1069 C) or a fibrillar decoration (arrows) in 89.2% of the EVs analyzed (panels D and E). Three-
1070 dimensional organization of the fibrillar decoration (yellow) on the membrane (purple) of
1071 EVs as revealed by cryo-electron tomography analysis (F), magnified in panels G and H. Full
1072 surface representation models as seen from top view (G). Same models clipped with clipping
1073 plane oriented perpendicular to line of sight (H). Data presented in this figure have been
1074 generated using images obtained using a Titan Krios (Thermo Scientific) transmission
1075 electron microscope.

1076

1077 **Figure 2: Analysis of size and structural diversity of *C. neoformans* EVs.**

1078 NTA analysis of purified EVs revealed a size diameter ranging from 80 to 500 nm, with the
1079 highest distribution around 150 nm (A). Frequency distribution of EV diameters determined
1080 by CryoEM, a total of 434 regular EVs were analyzed. The analysis based on CryoEM
1081 tomograms revealed a wider range of EV size distribution, from 10 to 500 nm diameter, with
1082 the highest relative frequency below 100 nm (B). Cryo-EM images exemplifying EV size
1083 range. Scale bars corresponding to 100 nm (C). EV size distribution according to the presence
1084 or absence of surface decoration (D). Non-decorated EVs have a smaller diameter size
1085 distribution compared to decorated ones (E). Analysis of decoration thickness from Cryo-EM
1086 images from 105 single EVs (F). Analysis of a potential relationship between decoration
1087 thickness and EV diameter by linear regression (G). Data presented in this figure have been
1088 generated using images obtained using a Titan Krios (Thermo Scientific) transmission
1089 electron microscope. Error bars show means \pm SD. Sample size (n) is indicated and, in
1090 brackets, the number of vesicles in that category that exceeded 500 nm in size.

1091

1092 **Figure 3: Comparative analysis of size and structural diversity of EVs in *C. neoformans*,**
1093 ***C. deneoformans* and *C. deuterogattii*.**

1094 Analysis of EV diameters revealed a smaller size distribution in *C. deuterogattii* strain R265
1095 and *C. deneoformans* strain JEC21 than in *C. neoformans* KN99α. The total numbers of

1096 vesicles analyzed were *C. neoformans* (n=143 for size and n=112 for decoration), *C.*
1097 *deneoformans* (n= 90 for size and n=63 for decoration), *C. deuterogattii* (n= 115 for size and
1098 n=95 for decoration) (A). Analysis of the decoration thickness revealed a smaller distribution
1099 for *C. deneoformans* and *C. deuterogattii* compared with *C. neoformans* (B). Illustrative
1100 images of size and decoration of EVs obtained from the three species. The data presented in
1101 this figure have been generated using images obtained using a TECNAI F20 transmission
1102 electron microscope (C). Error bars show means ± SD. Scale bars represent 100 nm.

1103

1104

1105 **Figure 4: Flow cytometry analysis of *C. neoformans* EVs incubated with monoclonal**
1106 **anti-GXM antibody.**

1107 FACS analysis of wild type (WT) and the acapsular *cap59Δ* EVs in PBS or in the presence of
1108 the monoclonal antibody raised against the capsular polysaccharide 18b7 (+ mAb anti-GXM)
1109 (A). The analysis revealed strong labelling of WT vesicles (74.7%), compared to the weak
1110 labelling in the mutant (2.33%), (B). Despite the important labelling difference, *C.*
1111 *neoformans* WT and *cap59Δ* strains released EVs bearing similar surface decoration, shown
1112 by the cryo-EM (arrows), as well as EVs obtained from other fungal species such as *C.*
1113 *albicans* and *S. cerevisiae* (C). These cryo-EM data have been generated using a TECNAI
1114 F20 transmission electron microscope. Scale bar represents 100 nm. This experiment was
1115 repeated twice with similar results.

1116

1117 **Figure 5: Analysis of *Cryptococcus* spp protein cargo.**

1118 Venn diagram revealing shared and unique EV-associated proteins in *C. neoformans*, *C.*
1119 *deneoformans*, and *C. deuterogattii*. Seventeen proteins were identified to be associated with
1120 EVs in all three *Cryptococcus* species (A). List of the gene loci and the corresponding
1121 proteins commonly found in EVs released by the three species, which could be considered as
1122 putative cryptococcal EV-protein markers (B). Most of the proteins are predicted to be either
1123 GPI-anchored proteins, to contain a signal peptide or to possess other membrane domains,
1124 according to preGPI, signalP and TMHMM website, respectively. Six protein families
1125 appeared to be typical of *Cryptococcus* EVs, including the Chitin deacetylase family (Cda),
1126 the Ricin-type beta-trefoil lectin domain-containing protein family (Ril), the putative glyoxal
1127 oxidase family (Gox), the tetraspanin membrane proteins containing a SUR7/PalI family
1128 motif (Tsh), the pr4/barwin domain protein family (Blp), and the multicopper oxidase (Cfo).
1129 Among these families, the proteins present in all three species are shown in green, proteins

1130 present in two species in orange and proteins present in only one species in yellow (C). We
1131 also identify 21 putative GPI-anchored proteins, as predicted by PredGPI, and 10 of them
1132 were present in all three species (D).

1133

1134 **Figure 6. Flow cytometry analysis of *C. neoformans* EVs incubated with GFP-labelled**
1135 **ConA.**

1136 FACS analysis of EVs obtained from *C. neoformans* wild type and *cap59Δ* cells. EVs were
1137 incubated with ConA-Alexa Fluor 488 conjugated lectin. After ultracentrifuge washing, the
1138 EV pellets were mixed in BD Trucount tubes (BD Biosciences), containing a known number
1139 of fluorescent beads as internal control. The number of events for each reading was fixed to
1140 100,000 events and the percentage and intensity of ConA labeling were recorded. This
1141 experiment was repeated three times with similar results.

1142

1143 **Figure 7. EV proteinase K treatment reduces ConA binding.**

1144 FACS analysis of EVs obtained from *C. neoformans* WT and *cap59Δ* cells after proteinase K
1145 treatment. Proteinase K-treated EVs were submitted to ConA labelling, ultracentrifuge
1146 washed and analyzed by flow cytometry. EV pellets were mixed in BD Trucount tubes (BD
1147 Biosciences), containing a known number of fluorescent beads as an internal control. The
1148 number of events for each reading was fixed to 100,000 events and the percentage and
1149 intensity of ConA labeling were recorded. EVs treated using the same protocol but omitting
1150 the enzyme were used as controls.

1151

1152 **Figure 8. Analysis of *C. neoformans* mutant strain EVs.**

1153 Evaluation of EV production by the different mutant strains as estimated by the measure of
1154 the sterol concentration using the Amplex™ Red Cholesterol Assay Kit (A). Impact of the
1155 different mutations on the percentage of ConA-labelled EVs as estimated through flow
1156 cytometry (B). Analysis of EV size diameter in the *mp88Δ* and *alg3Δ* mutant strains as
1157 compared to the wild type (WT). The total number of vesicles analyzed were WT (n = 143 for
1158 size and n = 112 for decoration), *mp88Δ* (n = 107 for size and n = 86 for decoration), *alg3Δ* (n
1159 = 119 for size and n = 92 for decoration) (C). Analysis of the decoration thickness revealed a
1160 smaller distribution associated with *ALG3* or *MP88* deletions, as exemplified by illustrative
1161 images from the three strains (D). The cryo-EM images were obtained using a TECNAI F20
1162 transmission electron microscope. ConA labelling and sterol measurements were done for at

1163 least three independent biological replicates Error bars are represented as means \pm SD. Scale
1164 bars represent 100 nm in C and 20 nm in D. (E)

1165

1166 **Figure 9: Model of simplified molecular structure and composition of *Cryptococcus* EVs.**

1167 In accordance with previous reports and in the light of our data, a new model of *Cryptococcus*
1168 EVs is suggested, where the outer layer is composed of the capsular polysaccharide
1169 glucuronoxylomannan (GXM), and the lipid bilayer is covered by many proteins, including
1170 mannoproteins, making the visible fibrillar structure resolved by cryo-EM. Most of the
1171 proteins are predicted to be GPI-anchored, to contain a signal peptide or to possess other
1172 membrane domains, according to preGPI, signalP and TMHMM, respectively. Three proteins,
1173 the hypothetical protein Cpc1, the putative V-type ATPase (Vma10) and the Vep3 are
1174 predicted to be soluble. It is still unclear if these proteins are indeed inside the vesicular lumen
1175 or linked to another transmembrane protein. For simplification, the lipid content was not
1176 explored, but previous works shown the presence of sterol, phospholipoids and sphingolipids.
1177 Additionally, *Cryptococcus* EVs were also described to contain other cargoes, such as RNA,
1178 pigments, small molecules, and polysaccharides, including GXM, as detailed in plain text.

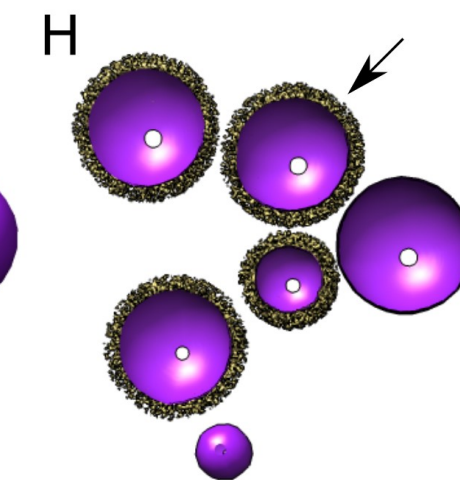
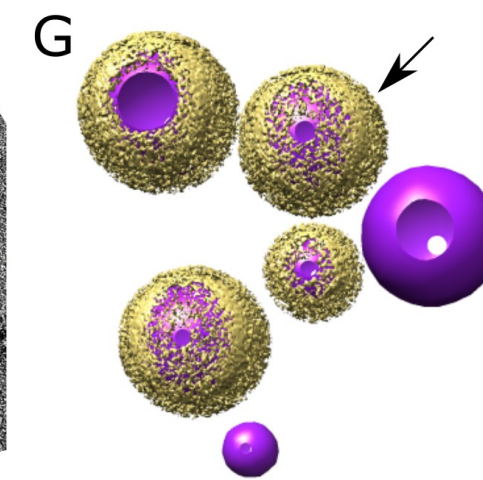
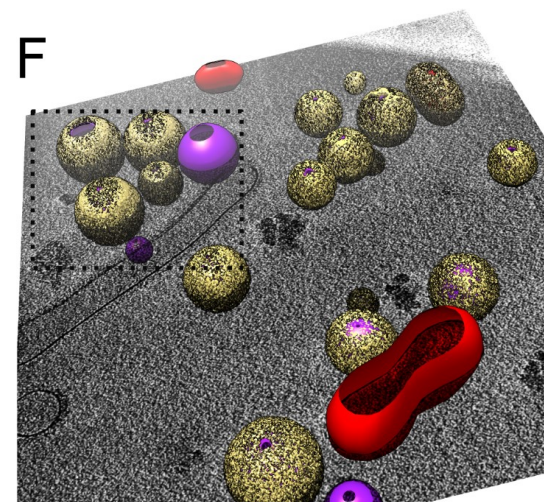
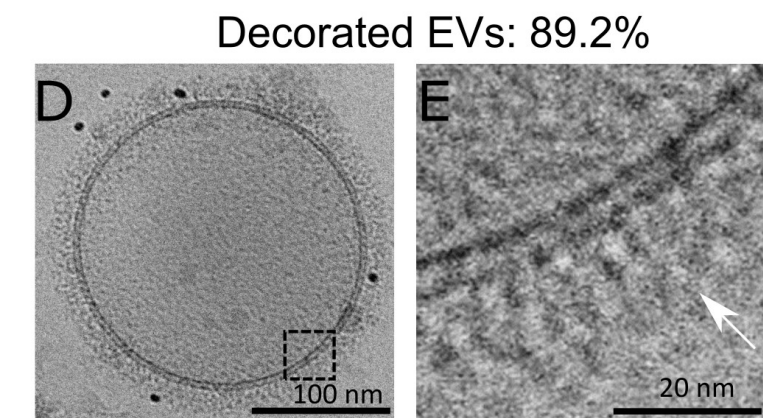
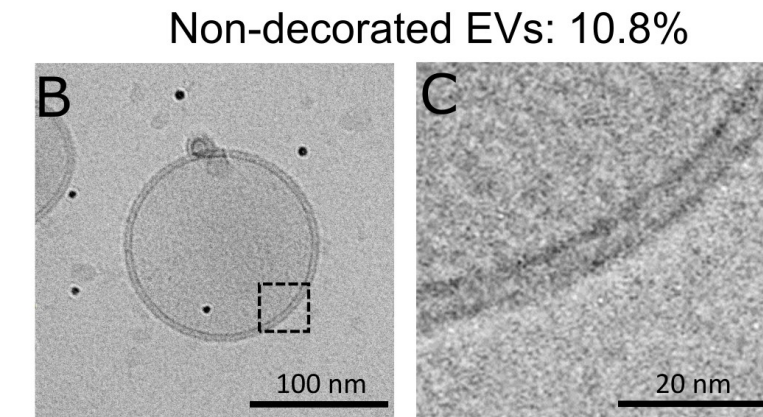
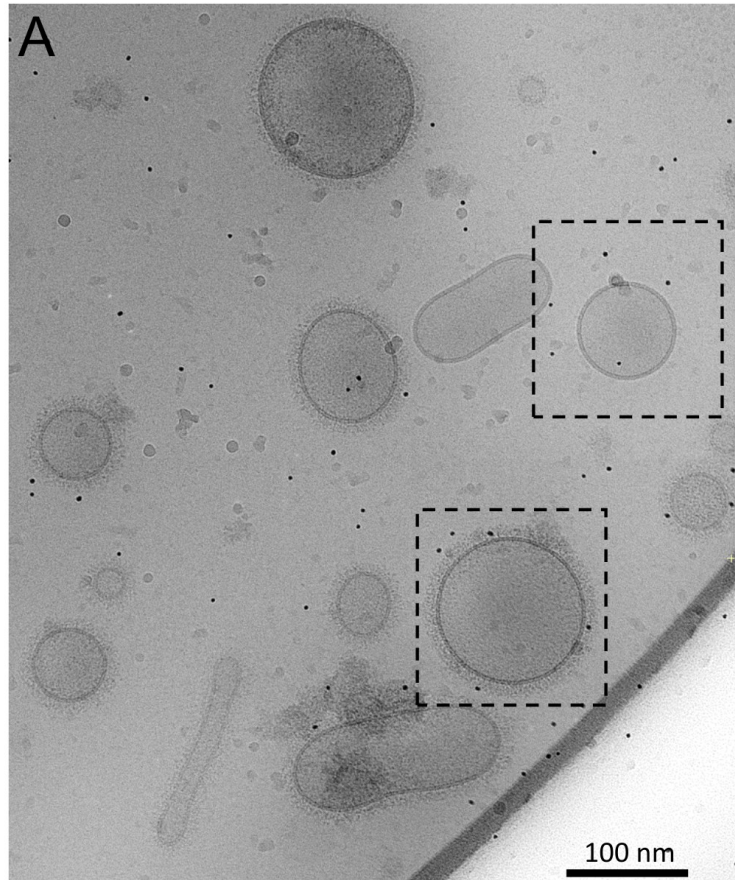
1179

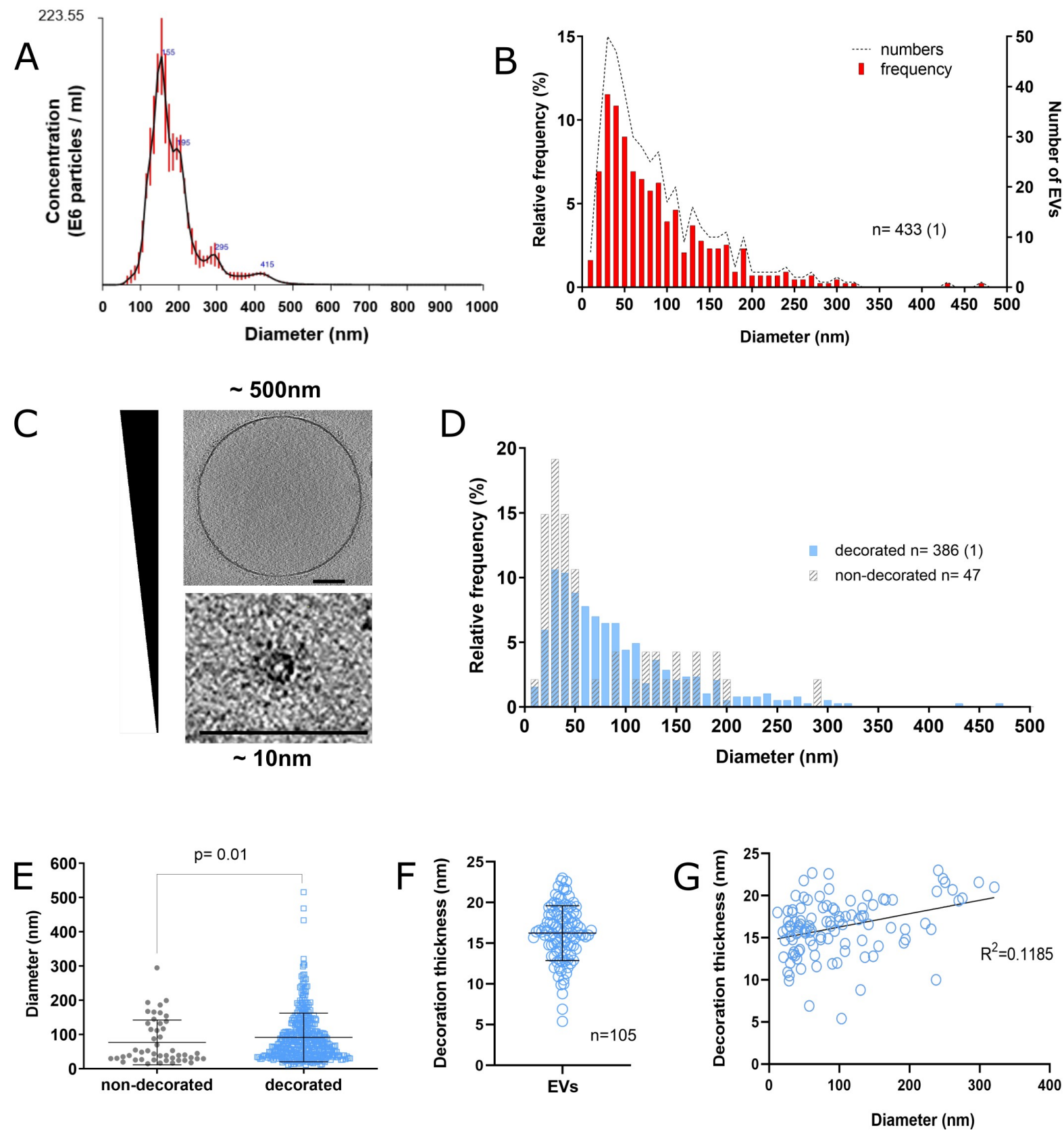
1180 **Figure 10. Vaccination assays using *C. neoformans* EVs.**

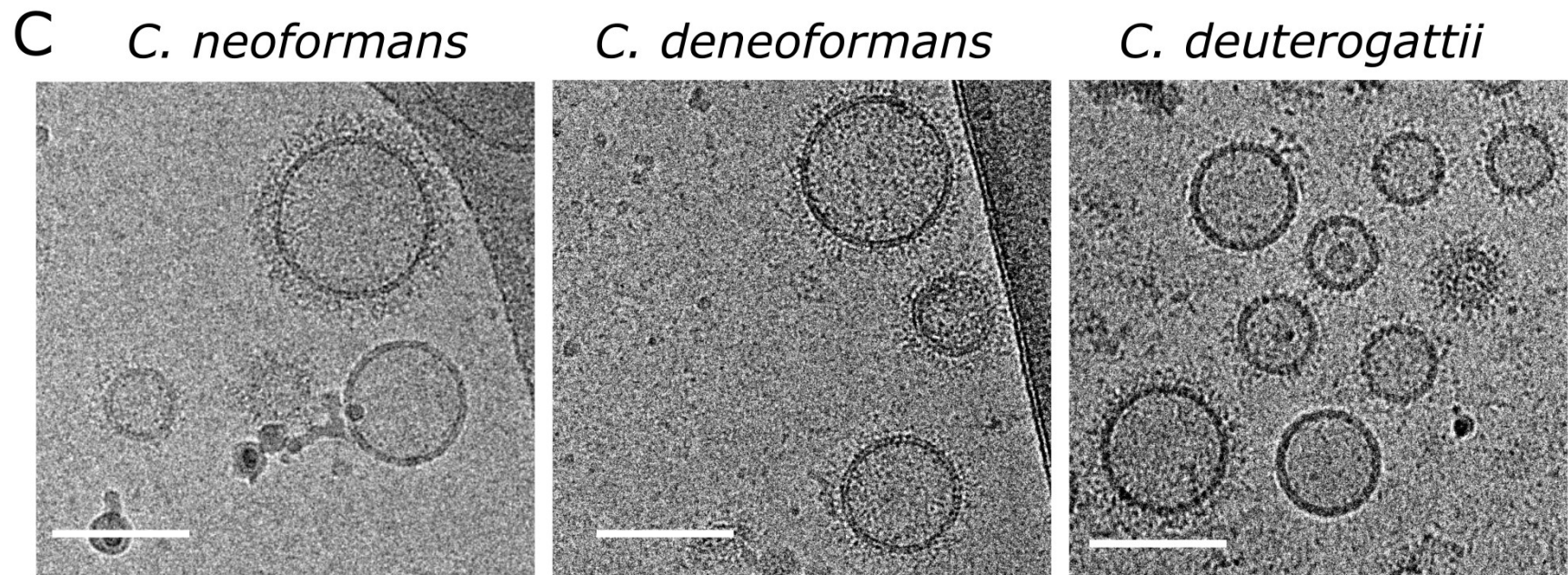
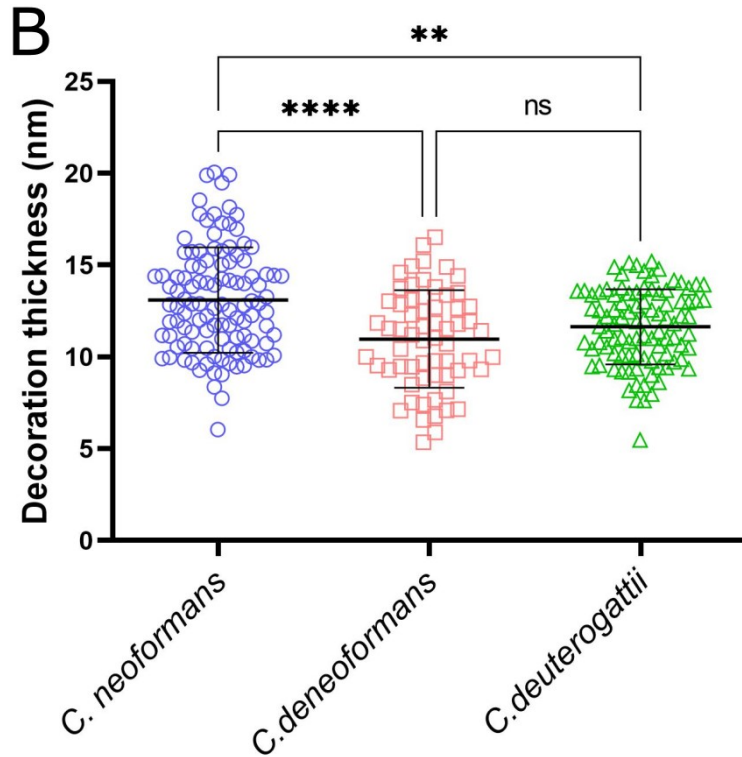
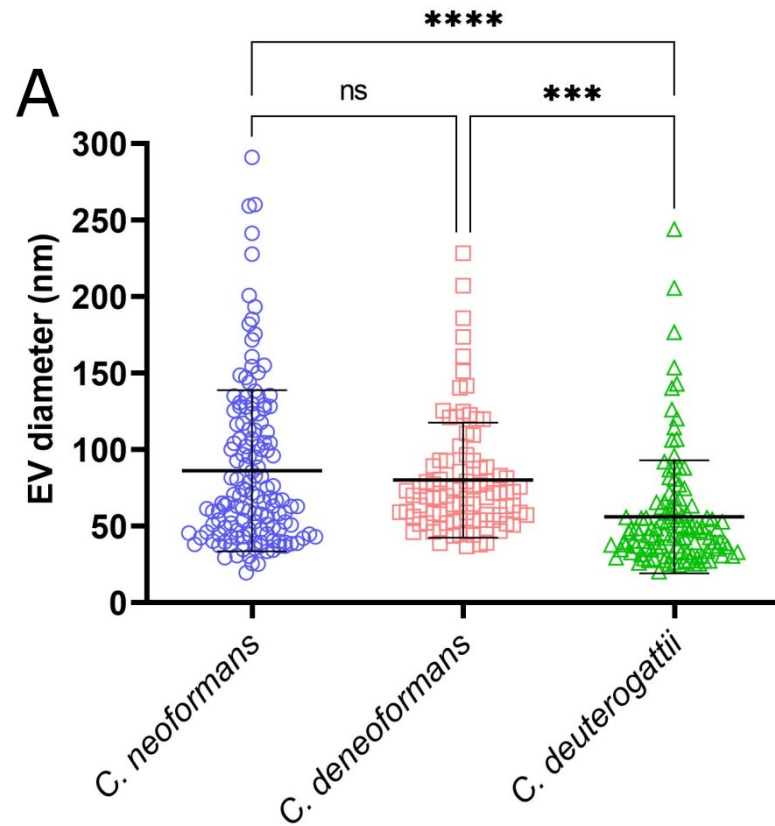
1181 Female 6-weeks old BALB/c mice were immunized with *C. neoformans* EVs via
1182 intraperitoneal injection, followed by intranasal infection with 1×10^4 yeasts of wild-type
1183 (WT) *C. neoformans*, and the mouse survival was monitored. In the first pilot experiment,
1184 mice (n = 4 per group) were immunized with EVs from wild type or *cap59Δ* strain (1 and 10
1185 μ g in 100 μ L of PBS) and control mice were injected with 100 μ L PBS. Western Blot using
1186 mouse sera against fungal EV confirmed that all immunized mice produced antibodies against
1187 EV proteins (A). All EV-immunized mice survived longer than the non-immunized ones, but
1188 the immunization with *cap59Δ* EVs rendered a significantly prolonged mouse survival ($*p =$
1189 0.01) (B). For the second set of experiment, mice (n = 10 per group) were immunized with
1190 EVs from *cap59Δ* mutant strain (10 μ g/100 μ L in PBS) and control mice were injected with
1191 100 μ L PBS. Again, Western blot using mouse sera against fungal EVs confirmed that all
1192 immunized mice produced antibodies against EV proteins(C). EV-immunized mice showed
1193 significantly prolonged survival ($*p = 0.0006$) compared to the non-immunized group (D).
1194 Comparison of the survival curves was made by GraphPad Prism 8, using the Log-rank
1195 (Mantel-Cox) test.

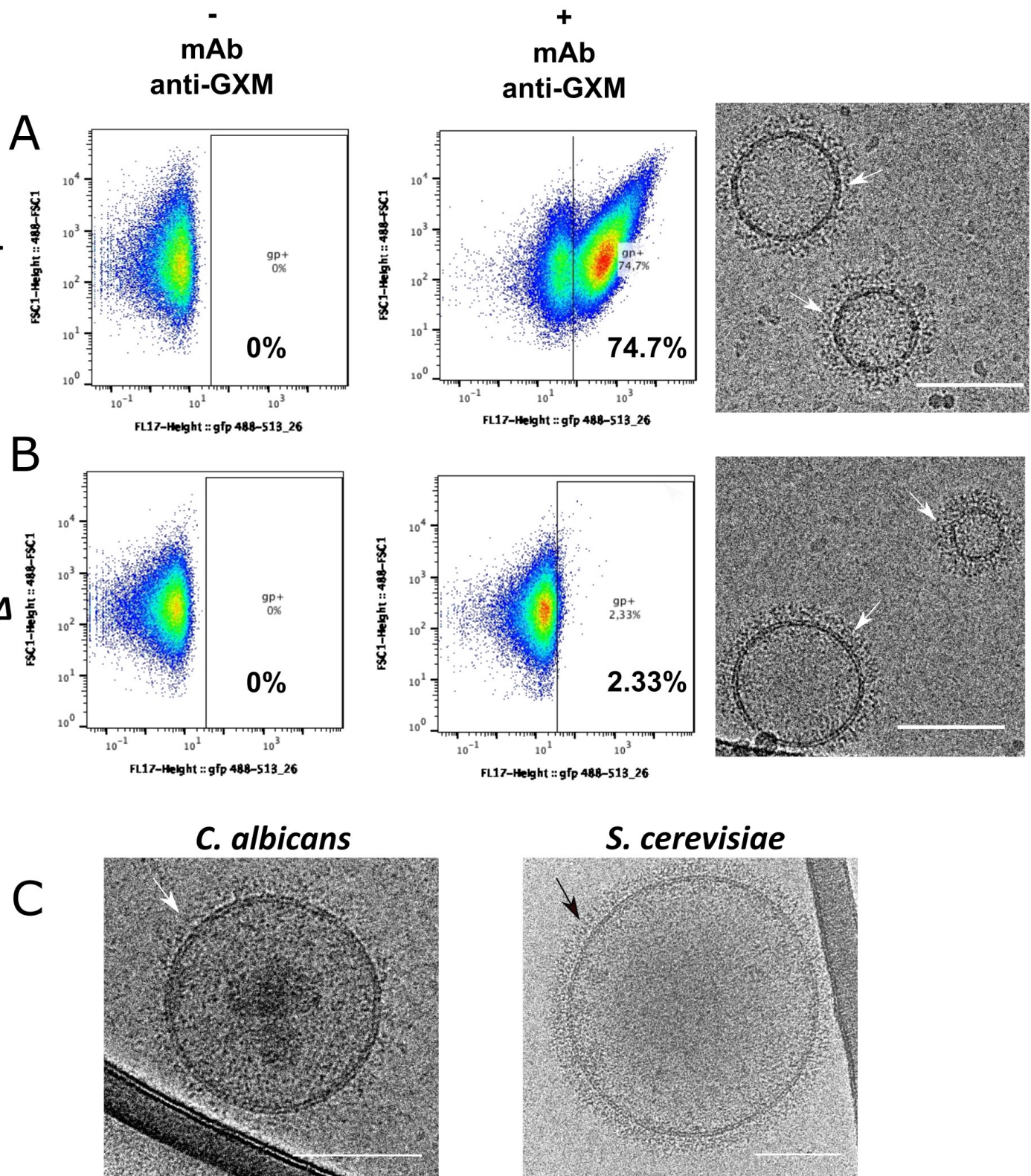
1196

1197

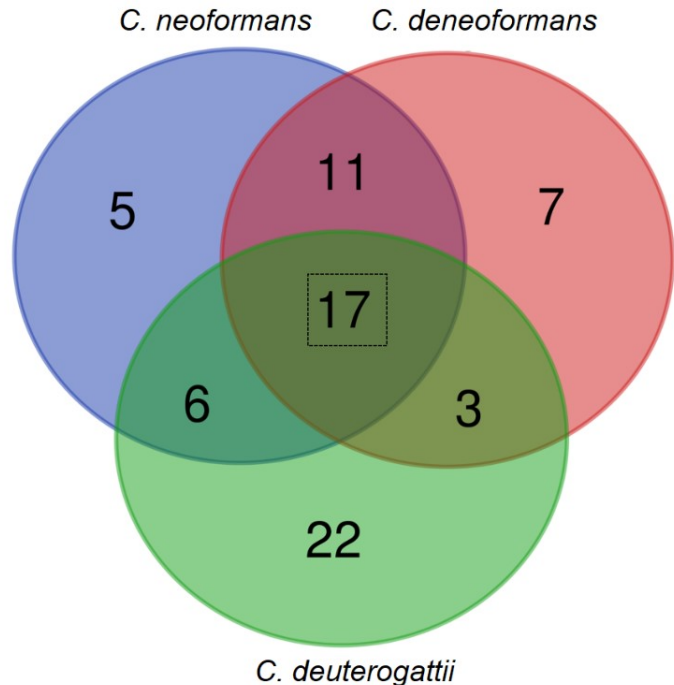








A

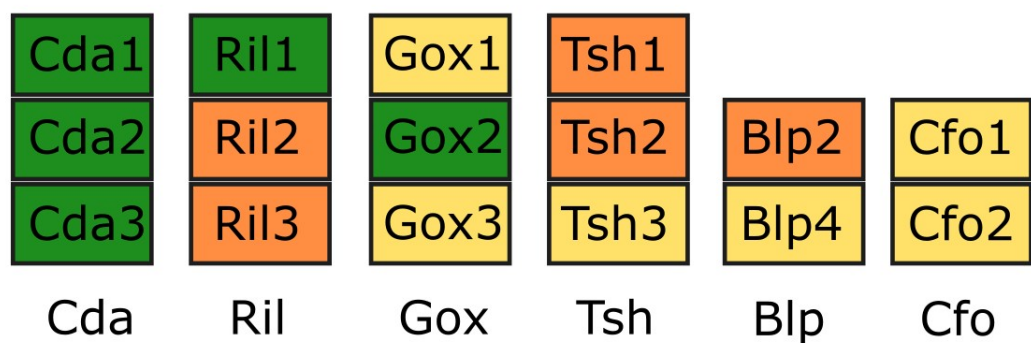


B

List of EV- enriched proteins shared by the three *Cryptococcus* spp.

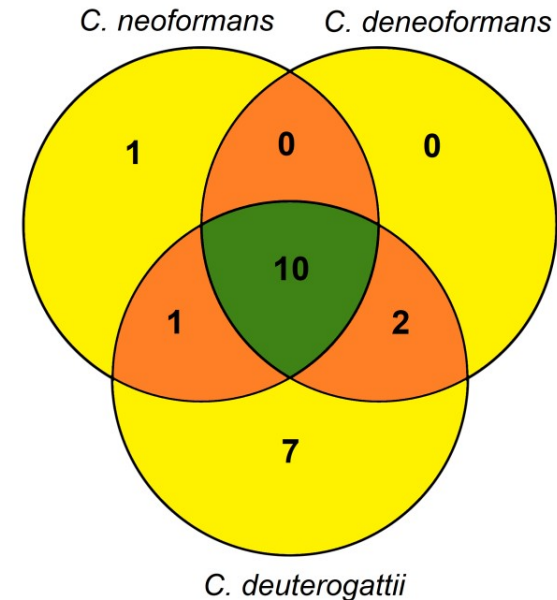
C. deuterogattii	C. deneoformans	C. neoformans	Protein name	Putative function
CNBG_1155	CNA07540	CNAG_00776	Mp88	Immunoreactive mannoprotein
CNBG_3648	CNC06180	CNAG_03007	Cpc1	DUF3759
CNBG_3432	CNC03950	CNAG_02775	Bim1	BCS-inducible membrane protein
CNBG_9064	CND03490	CNAG_01230	Mp98/Cda2	Chitin deacetylase
CNBG_5182	CNE05040	CNAG_02030	Gox2	Glyoxal oxidase
CNBG_3374	CNC03380	CNAG_01854	Hep2	Heparinase II/III family protein
CNBG_1745	CNF01800	CNAG_05799	Cda1	Chitin deacetylase
CNBG_4970	CNN02260	CNAG_06501	Gas1	1,3-Beta-glucanosyltransferase
CNBG_5817	CNJ03160	CNAG_04891	Ril1	Ricin-type beta-trefoil lectin domain-containing protein
CNBG_4258	CNH02560	CNAG_05615	Sso1	t-SNARE complex subunit
CNBG_9173	CNF01900	CNAG_05788	Vma10	V-type ATPase, G subunit
CNBG_5332	CNE03480	CNAG_02189	Amy1	Alpha-amylase
CNBG_4145	CNE01150	CNAG_02443	Vep3	NADH dehydrogenase
CNBG_5365	CNE03150	CNAG_02225	Exg104	Glucan 1,3-beta-glucosidase
CNBG_0679	CND02350	CNAG_01109	Vep4	Hypothetical protein
CNBG_0806	CND03580	CNAG_01239	Cda3	Chitin deacetylase
CNBG_5038	CNN01470	CNAG_06422	Vep5	Hypothetical protein

C



Protein families

D

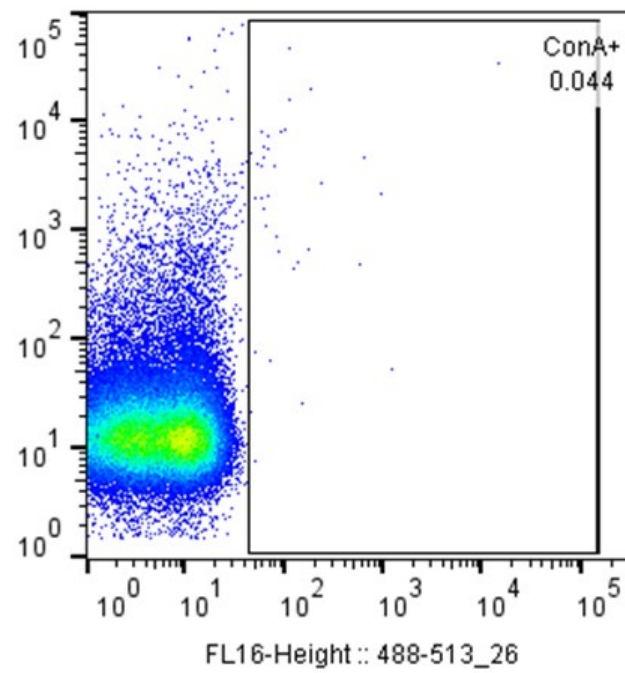
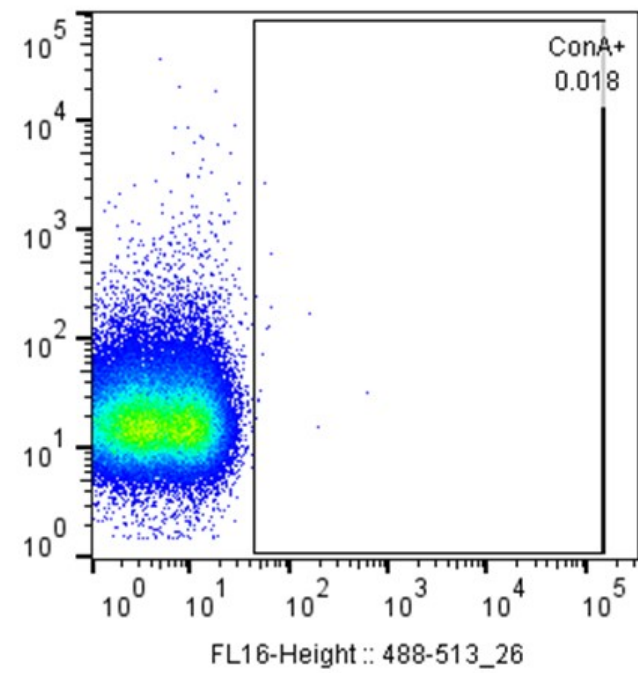
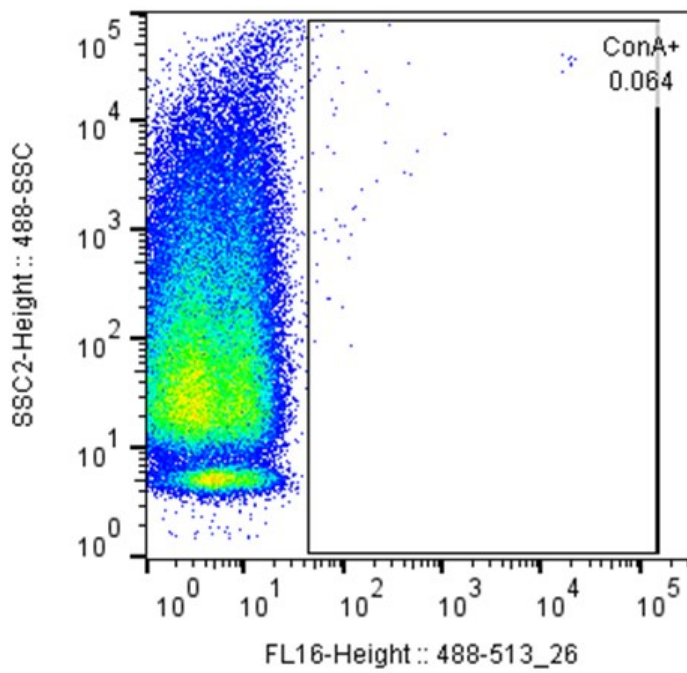


PBS

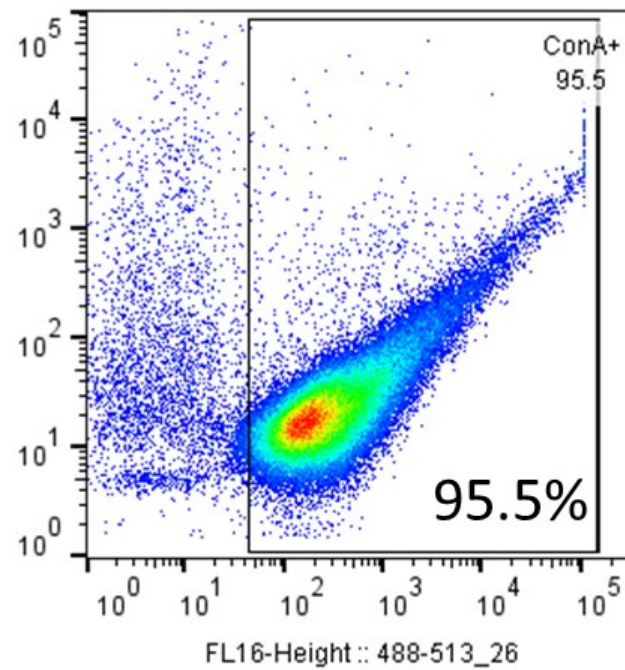
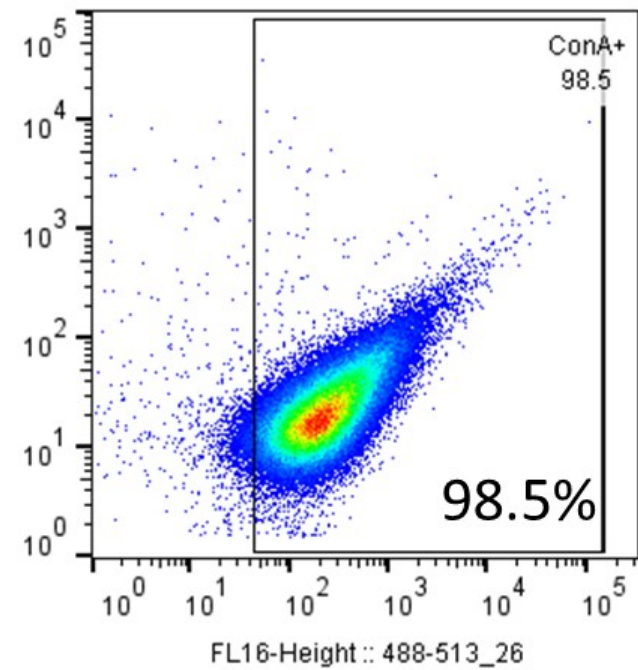
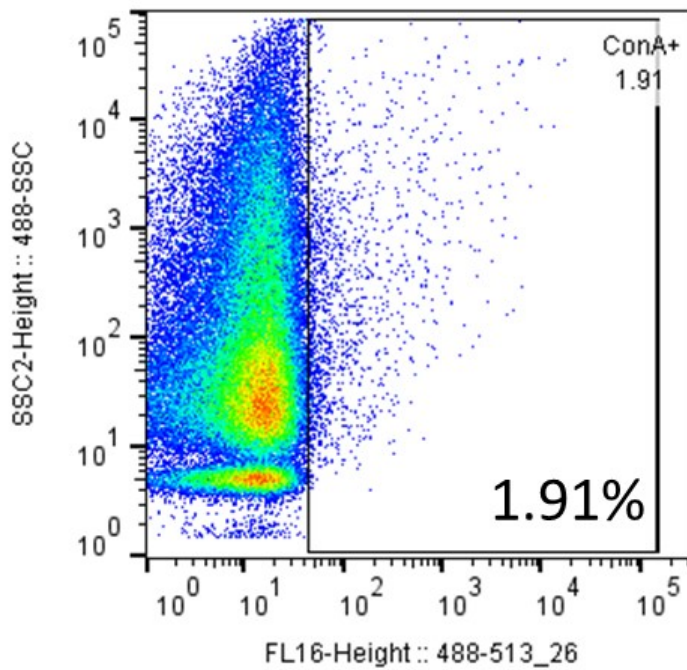
WT

cap59Δ

- ConA

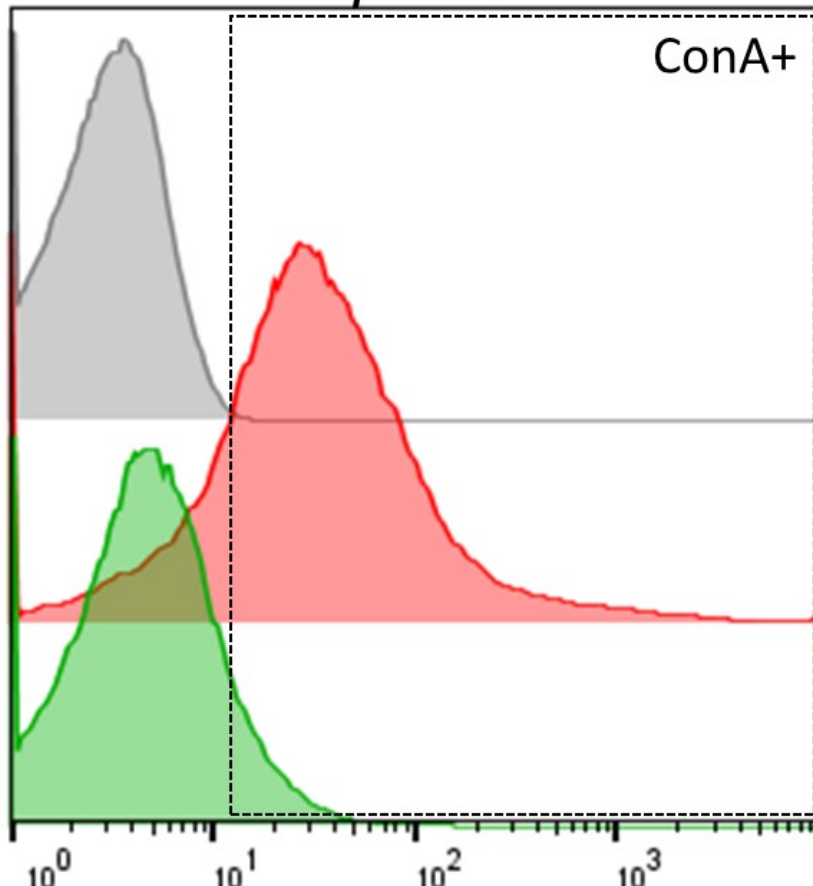
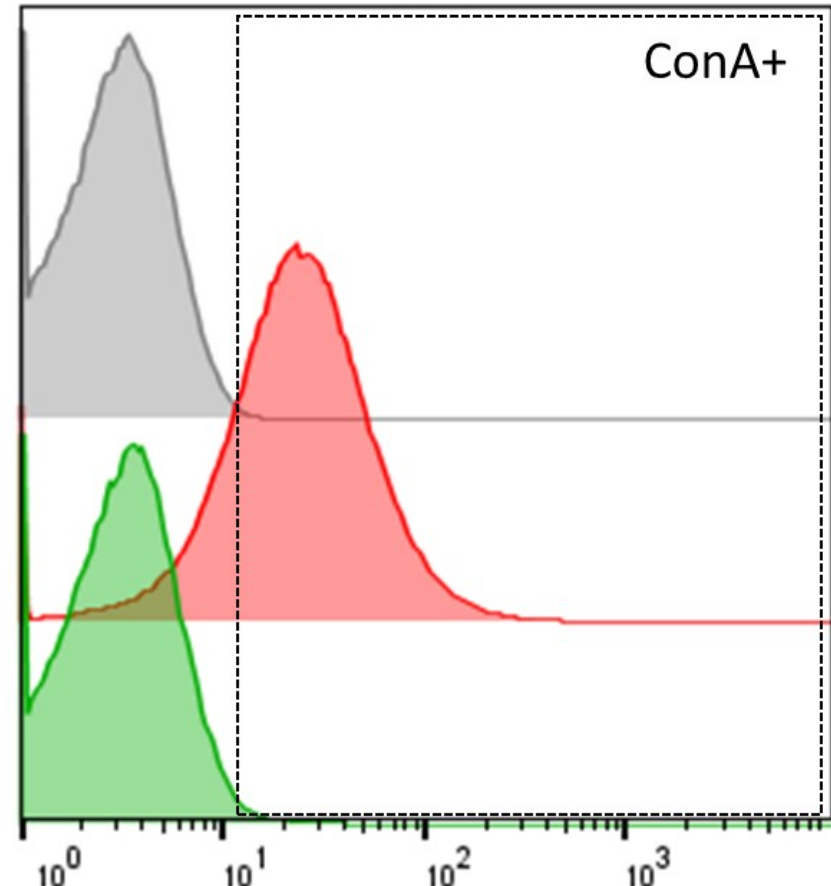


+ ConA



WT

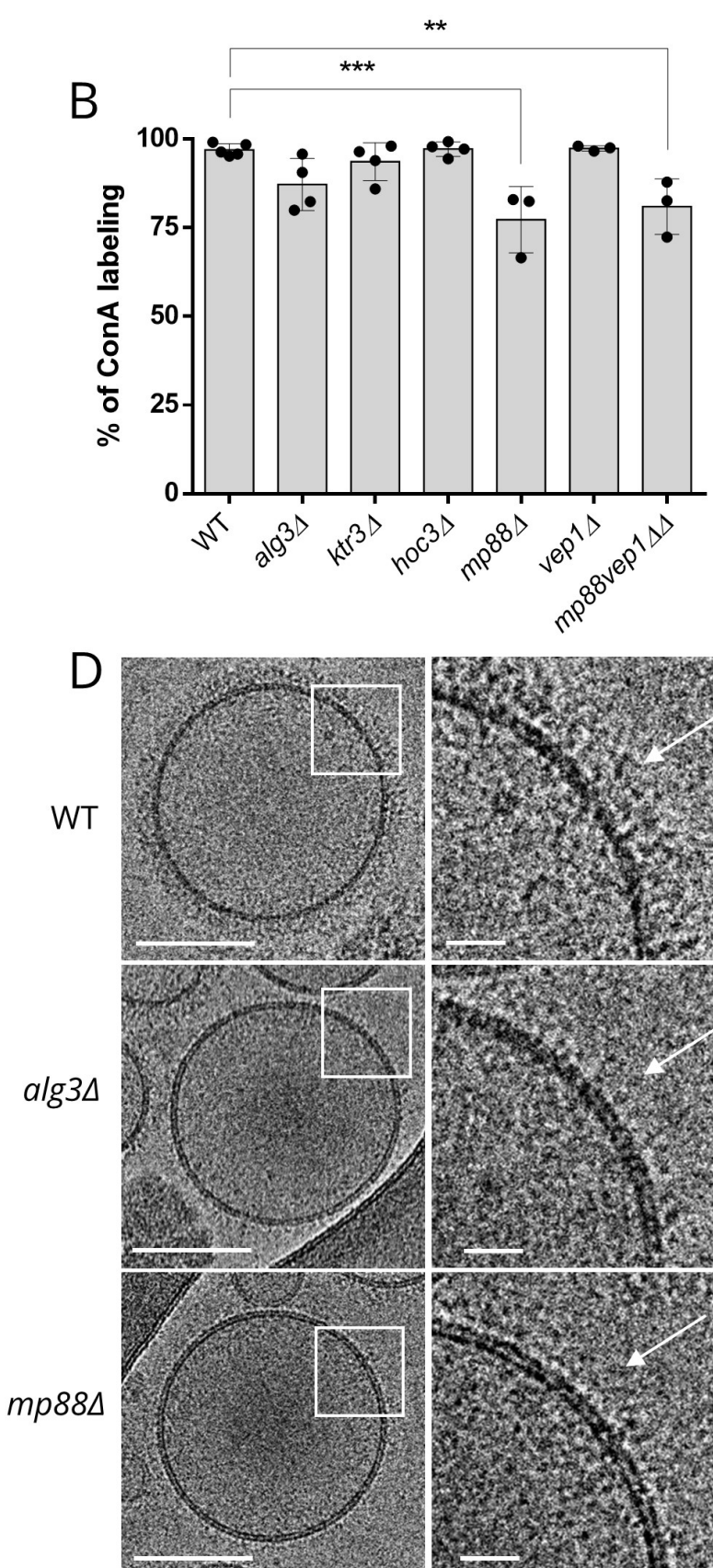
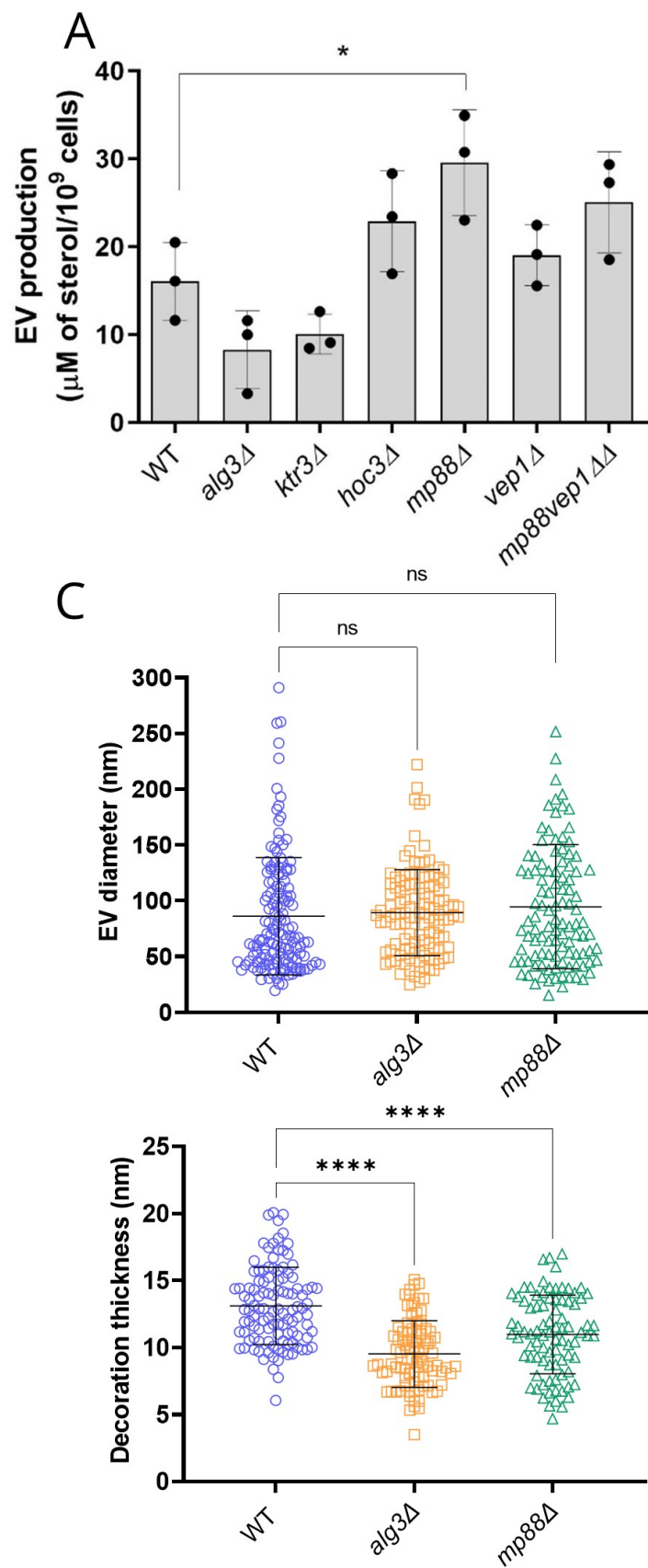
cap59Δ

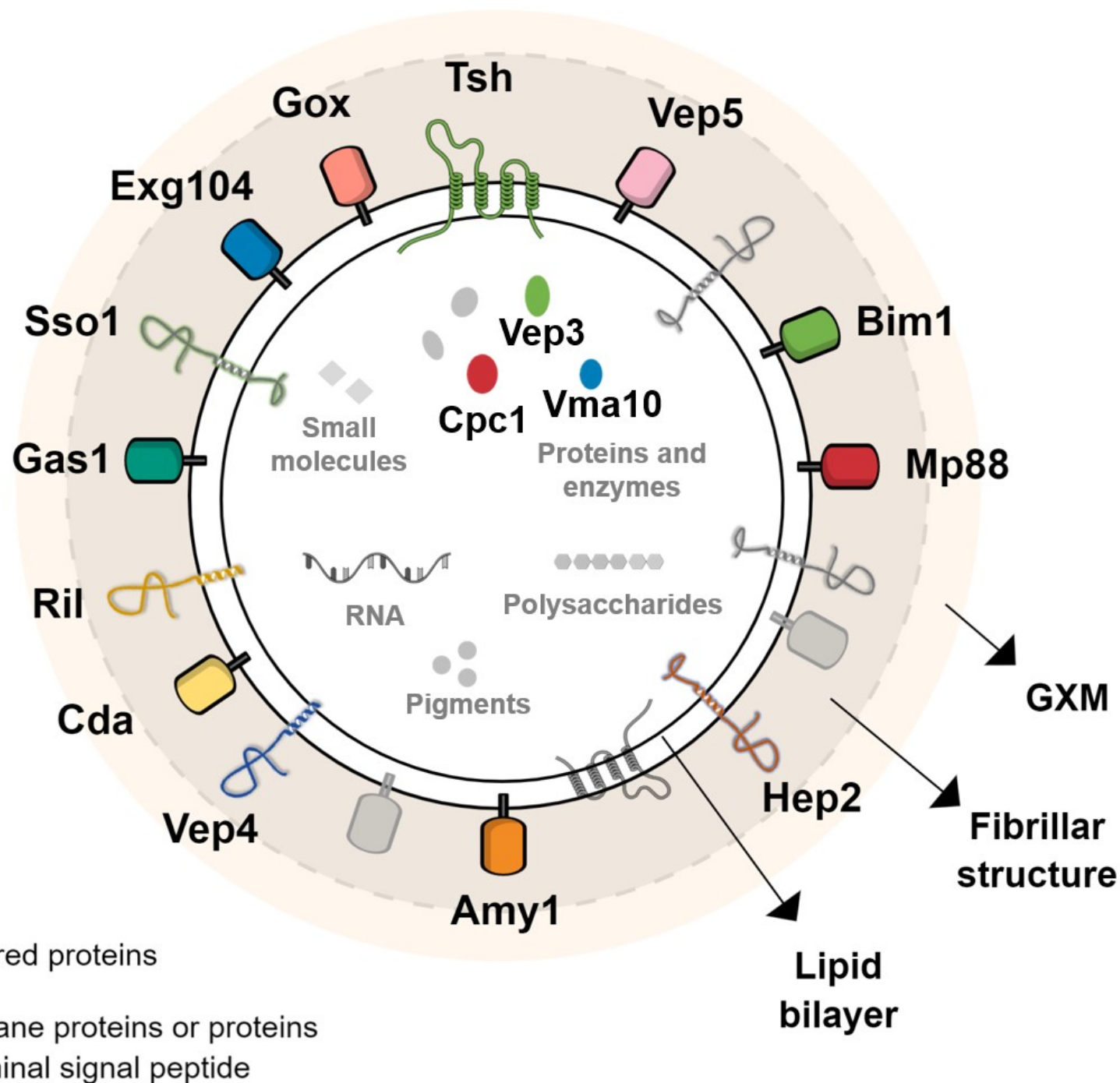


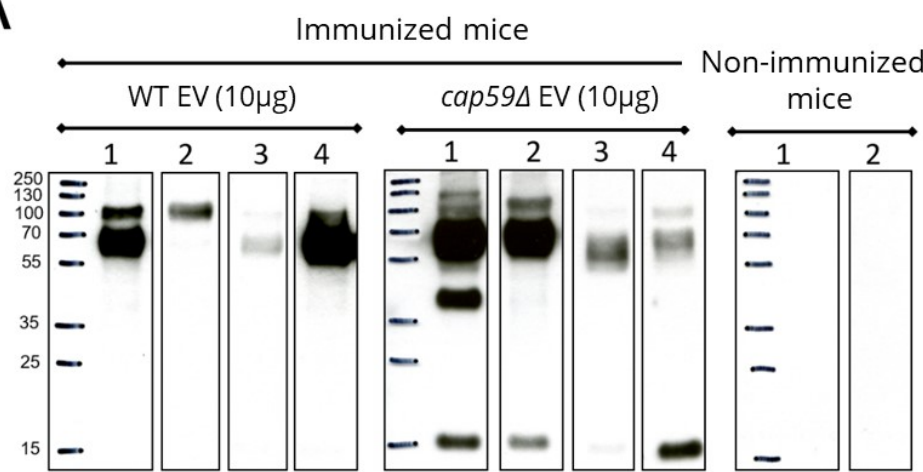
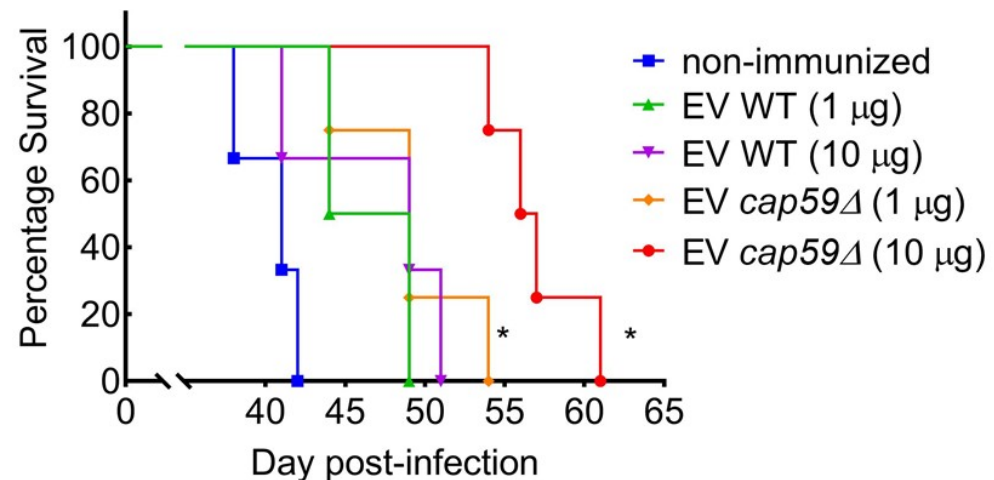
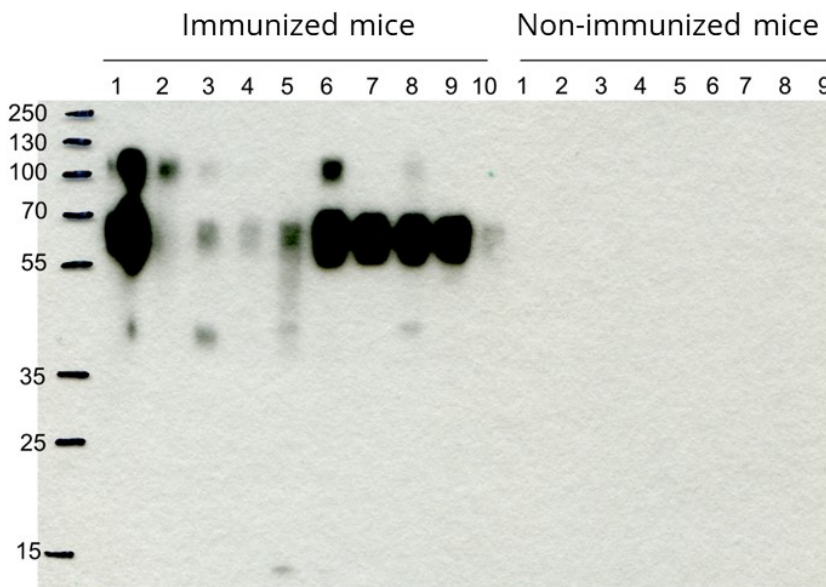
EVs

EVs + ConA

EVs + PK+ ConA





A**B****C****D**